Available online at www.sciencedirect.com
ScienceDirect
Journal of Computational Physics 227 (2008) 7368–7393
JOURNAL OF COMPUTATIONAL PHYSICS
www.elsevier.com/locate/jcp

High order central scheme on overlapping cells for magneto-hydrodynamic flows with and without constrained transport method

Shengtai Li *

Theoretical Division, MS B284, Los Alamos National Laboratory, Los Alamos, NM 87545, United States

Received 27 November 2007; received in revised form 18 March 2008; accepted 22 April 2008
Available online 6 May 2008

Abstract

This paper extends the central finite-volume schemes of Liu et al. [Y. Liu, C.-W. Shu, E. Tadmor, M. Zhang, Non-oscillatory hierarchical reconstruction for central and finite-volume schemes, Commun. Comput. Phys. 2 (2007) 933–963] on overlapping cells to the magneto-hydrodynamic (MHD) equations. In particular, we propose a high order divergence-free reconstruction for the magnetic field that uses the face-centered values. We also advance the magnetic field with a high order constrained transport (CT) scheme to preserve the divergence-free condition to machine round-off error. The overlapping cells are natural to be used to calculate the electric field flux without an averaging procedure. We have developed a third-order scheme which is verified by the numerical experiments. Other higher order schemes can be constructed accordingly. Our central constrained transport schemes do not need characteristic decomposition, and are easy to code and combine with un-split discretization of the source and parabolic terms. The overlapping cell representation of the solution is also used to develop more compact reconstruction and less dissipative schemes. The high resolution is achieved by non-oscillatory hierarchical reconstruction, which does not require characteristic decomposition either. The numerical comparisons show that the central schemes with non-CT perform as well as with CT for most of problems. Numerical examples are given to demonstrate efficacy of the new schemes.
Published by Elsevier Inc.

Keywords: Central schemes; High order; Non-oscillatory; Constrained transport (CT); Divergence-free reconstruction; Overlapping cell; Magneto-hydrodynamics (MHD)

1. Introduction

In recent years there has been substantial progress in numerical magneto-hydrodynamics (MHD) based on high-order Godunov methods. Early development of high-order Godunov schemes for MHD focused on interpreting the MHD equations as a simple system of conservation laws. More recent efforts have focused

* Tel.: +1 505 665 8407; fax: +1 505 665 5757.
E-mail address: sli@lanl.gov

0021-9991/$ - see front matter Published by Elsevier Inc.
doi:10.1016/j.jcp.2008.04.022

on divergence-free evolution of the magnetic field. Brackbill and Barnes [8] recognized that the Lorentz force is not orthogonal to the magnetic field if the divergence-free condition is not satisfied, and that this could lead to incorrect dynamics. Several approaches have been proposed to handle this problem. The first is to use a Hodge projection to clean the magnetic field of any divergence after each time step (see [29] and its reference). Balsara and Kim [6] find that the divergence-cleaning is significantly inadequate when used for many astrophysical applications. Powell [24] transformed the MHD equations into a well-posed eight-wave system by adding source terms proportional to divergence of the magnetic field ($\nabla \cdot \mathbf{B}$). Then nonphysical numerical magnetic monopole is advected away according to the new formulation. Yet another approach has been proposed by Dedner et al. [11] to damp the divergence errors while convecting it away by adding diffusion to the hyperbolic convection of the $\nabla \cdot \mathbf{B}$. The *constrained transport* (CT) approach uses a staggered grid which places the magnetic field variables at the cell-face to keep machine round-off error. Recently, this approach has been combined with various high resolution shock-capturing (HRSC) schemes by many authors, e.g. [3,10,21,27,29].

Many HRSC schemes require full information about the eigen-structure of the underlying system either to solve the Riemann problem at cell interfaces or for characteristic decomposition. The central schemes, on the other hand, usually do not need characteristic decomposition. The simplest example is the Lax-Friedrichs (LxF) scheme, which is only of first-order and very dissipative. The central scheme of Nessyahu and Tadmor (NT) [23] provides a second-order generalization of the staggered LxF scheme. High resolution generalizations of the NT scheme were developed since 90s as the class of central schemes in e.g. [13,15,19]. All of the high order schemes require a high order reconstruction of the solutions. When the reconstruction order becomes higher, characteristic decomposition is usually necessary to reduce the spurious oscillations (see [25]). Liu et al. [18] proposed a hierarchical non-oscillatory reconstruction to remove the spurious oscillations while maintaining the high resolution without characteristic decomposition.

The CT approach is based on a staggered collocation of the magnetic and electric field components and employs a special discretization such that the divergence of the curl of the electric field vanishes numerically. Most of the CT methods rely on constructing the electric field by averaging the information obtained from solving the cell-average values of the solutions (e.g. [3,5,10,27,29]) when combining with a HRSC scheme. Due to the averaging, some 2D CT schemes (e.g. [3,10]) cannot be reduced to the equivalent 1D solver for plane-parallel grid aligned flow. Gardiner and Stone [12] proposed a general approach to evaluate the electric field so that the CT scheme will recover the 1D solution for planar, grid-aligned flows. These CT schemes still used the fluxes obtained from the Godunov step but differed in their dissipation properties for truly multi-dimensional flows.

In this paper, we consider to apply the high order central schemes on the overlapping cells to the MHD flows. The combination of the second order central scheme with the flux-CT of Balsara and Spicer [3] was described by Ziegler [32]. Londrillo and Del Zanna [21] have combined the third order convex ENO (CENO) scheme of Liu and Osher [20] with their proposed upwind CT scheme. A third-order central scheme based on semi-discrete formulation for the nonstaggered grid is also proposed in Balbás and Tadmor [1]. A fully discrete second-order version using the staggered grid was presented in [2]. Our method differs from theirs in: (a) our base scheme is the central scheme on overlapping cells, which is quite different from the schemes on non-staggered grid; (b) we have proposed a third-order CT scheme without any averaging by using the overlapping cell information; (c) we have used the non-oscillatory hierarchical reconstruction to achieve the TVD properties; and (d) we have constructed a high order (third or higher) divergence-free reconstruction for the magnetic field using only the face-centered magnetic field.

As noted in [1], the divergence error of the magnetic field in central schemes without CT is relatively smaller than that in the upwind-type schemes. The constraint $\nabla \cdot \mathbf{B} = 0$ is even preserved numerically for the second-order staggered implementation of the central schemes (see [1,2]). Our numerical results in Section 4 also show that the central schemes on overlapping grid without CT work as well as with CT for most of the examples.

The outline of the paper is as follows. In Section 2, we review the central schemes on overlapping cells and propose a central scheme for the face-centered magnetic field. In Section 3, we derive two third-order divergence-free reconstructions for the magnetic field with and without the combined cell information. Several examples are given in Section 4, demonstrating the effectiveness of our scheme.

2. Central schemes on overlapping cells

2.1. Central schemes for the cell-average values

For the sake of a self-contained presentation we summarize the central scheme presented by Liu et al. [18]. Consider a system of conservation law

$$\frac{\partial \mathbf{u}}{\partial t} + \nabla \cdot \mathbf{F}(\mathbf{u}) = 0 \tag{1}$$

where $\mathbf{u} = (u_1, \ldots, u_m)^{\mathrm{T}}$. For simplicity, we assume a uniform staggered rectangular mesh depicted in Fig. 1 for the 2D case. Let $\{C_{I+1/2}\}, I = i_1, i_2, \ldots, i_d$ be a partition of R^d into uniform square cells depicted by solid lines in Fig. 1 and tagged by their cell centroids at the half integers, $\mathbf{x}_{I+1/2} := (I + 1/2)\Delta x$. Let $\overline{U}_{I+1/2}(t)$ be the numerical cell average approximating $(1/|C_{I+1/2}|)\int_{C_{I+1/2}} u(\mathbf{x}, t)\,\mathrm{d}\mathbf{x}$, in particular, $\overline{U}^n_{I+1/2} = \overline{U}_{I+1/2}(t^n)$. We will denote these cells as U-cell subsequently. Let $\{D_I\}$ be the dual mesh which consists of a $\Delta x/2$-shift of the $C_{I+1/2}$'s depicted by dash lines in Fig. 1. Let $\mathbf{x}_I$ be the cell centroid of the cell D_I. Let $V_I(t)$ be the numerical cell average approximating $(1/|D_I|)\int_{D_I} u(\mathbf{x}, t)\,\mathrm{d}\mathbf{x}$. We will refer these cells as V-cells. The semi-discrete central scheme on overlapping cells can be written as follows (for detailed derivation, see [17,18]):

$$\frac{\mathrm{d}}{\mathrm{d}t}\overline{U}_{I+\frac{1}{2}}(t^n) = \frac{1}{\Delta\tau^n}\left(\frac{1}{|C_{I+\frac{1}{2}}|}\int_{C_{I+\frac{1}{2}}} V^n(\mathbf{x})\,\mathrm{d}\mathbf{x} - \overline{U}^n_{I+\frac{1}{2}}\right) - \frac{1}{|C_{I+\frac{1}{2}}|}\int_{\partial C_{I+\frac{1}{2}}} \mathbf{f}(V^n(\mathbf{x}))\cdot\mathbf{n}\mathrm{d}s, \tag{2}$$

$$\frac{\mathrm{d}}{\mathrm{d}t}\overline{V}_I(t^n) = \frac{1}{\Delta\tau^n}\left(\frac{1}{|D_I|}\int_{D_I} U^n(\mathbf{x})\,\mathrm{d}\mathbf{x} - \overline{V}^n_I\right) - \frac{1}{|D_I|}\int_{\partial D_I} \mathbf{f}(U^n(\mathbf{x}))\cdot\mathbf{n}\mathrm{d}s. \tag{3}$$

where $\Delta\tau^n$ is a parameter dictated by the CFL condition ($\Delta\tau^n = (\text{CFL factor}) \times \Delta x/(\text{maximum characteristic speed})$), $U^n(\mathbf{x})$ and $V^n(\mathbf{x})$ are higher-oder piecewise polynomial approximation on cells $C_{I+1/2}$ and D_I respectively. The actually time step-size, Δt, can be much smaller than $\Delta\tau$ for convection-diffusion equations. The introduction of $\Delta\tau$ avoids the $O(1/\Delta t)$ dependence of the dissipation (see [17]) when $\Delta t \to 0$. To achieve the high order accuracy, the integrals on the right-hand side of Eqs. (2) and (3) must be evaluated by high order quadrature rule. The volume-integral is obtained by integrating the high-order reconstruction polynomial exactly. The face-integral of the flux is evaluated by either Gaussian or other high-order quadrature rule.

2.2. Ideal magneto-hydrodynamics (MHD) equations

The ideal MHD equations in conservative form can be written as

$$\rho_t + \nabla\cdot(\rho\mathbf{v}) = 0,$$
$$(\rho\mathbf{v})_t + \nabla\cdot\left[\rho\mathbf{v}\mathbf{v}^{\mathrm{T}} + p\mathbf{I} - \mathbf{B}\mathbf{B}^{\mathrm{T}}\right] = 0,$$

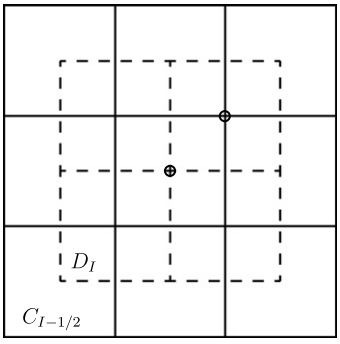

Fig. 1. Illustration of the overlapping cells. Both the primal grid (solid line) and the overlapping grid (dashed line) cover the whole domain.

$$\mathbf{B}_t - \nabla \cdot (\mathbf{v}\mathbf{B}^{\mathrm{T}} - \mathbf{B}\mathbf{v}^{\mathrm{T}}) = 0,$$
$$E_t + \nabla \cdot [(E+p)\mathbf{v} - \mathbf{B}(\mathbf{v}\cdot\mathbf{B})] = 0, \tag{4}$$

where ρ is density, $\mathbf{v}$ is the velocity, $\mathbf{B}$ is the magnetic field, $\mathbf{I}$ is the 3×3 unit tensor, E is the total energy per unit volume, and $p = p_{\mathrm{gas}} + \mathbf{B}\cdot\mathbf{B}/2$ is the total pressure, where p_{gas} is the gas pressure that satisfies the equation of state,

$$p_{\mathrm{gas}} = (\gamma-1)\left(E - \frac{1}{2}\rho\mathbf{v}\cdot\mathbf{v} - \frac{1}{2}\mathbf{B}\cdot\mathbf{B}\right),$$

and γ is the adiabatic index for the ideal plasma. One external constraint for magnetic field is the *divergence-free* condition $\nabla\cdot\mathbf{B} = 0$.

2.3. Divergence error for the central scheme on overlapping grid

We now quantify the divergence error of the magnetic fields for the central schemes (2) and (3). We use the U-cells as an example. The induction equation for the magnetic field is

$$\frac{\partial \mathbf{B}}{\partial t} = -\nabla\cdot\mathbf{E}, \tag{5}$$

where the electric field $\mathbf{E}$ is defined by $\mathbf{E} = -\mathbf{v}\times\mathbf{B} + \eta\mathbf{J}$, $\mathbf{v}$ is the velocity, $\mathbf{J} = \nabla\times\mathbf{B}$ is the current density, η is the resistivity. For ideal MHD, $\eta = 0$. From now on, we will consider only the ideal MHD in this paper. For a 2D MHD problem, Eq. (5) becomes

$$\frac{\partial B_x}{\partial t} = -\frac{\partial E_z}{\partial y}, \quad \frac{\partial B_y}{\partial t} = +\frac{\partial E_z}{\partial x}, \tag{6}$$

where $E_z = -(v_x B_y - v_y B_x)$. For the second-order discretization, we apply the trapezoidal rule to the face-integral in (2) and (3), and then the discretization of Eq. (6) becomes

$$\frac{\mathrm{d}}{\mathrm{d}t}\overline{B}^{U}_{x,i+1/2,j+1/2}(t^n) = \frac{1}{\Delta\tau^n}\left(\overline{B}^{V^n}_{x,i+1/2,j+1/2} - \overline{B}^{U^n}_{x,i+1/2,j+1/2}\right) - \frac{1}{2\Delta y}\left(E^V_{i,j+1} + E^V_{i+1,j+1} - E^V_{i,j} - E^V_{i+1,j}\right)$$
$$\frac{\mathrm{d}}{\mathrm{d}t}\overline{B}^{U}_{y,i+1/2,j+1/2}(t^n) = \frac{1}{\Delta\tau^n}\left(\overline{B}^{V^n}_{y,i+1/2,j+1/2} - \overline{B}^{U^n}_{y,i+1/2,j+1/2}\right) + \frac{1}{2\Delta x}\left(E^V_{i+1,j} + E^V_{i+1,j+1} - E^V_{i,j} - E^V_{i,j+1}\right)$$

where $E^V_{i,j}$ is a point-wise value at the cell-center of the V-cell D_I, and $\overline{B}^{V^n}_{*,i+1/2,j+1/2}$ is the sum of the integral of the reconstruction polynomials on four V-cells that cover the U-cell $C_{I+\frac{1}{2}}$. If the cell corner centered divergence is defined as (see also in [29])

$$(\nabla\cdot\mathbf{B})_{i,j} = \frac{\overline{B}_{x,i+1/2,j+1/2} + \overline{B}_{x,i+1/2,j-1/2} - \overline{B}_{x,i-1/2,j+1/2} - \overline{B}_{x,i-1/2,j-1/2}}{2\Delta x} + \frac{\overline{B}_{y,i+1/2,j+1/2} + \overline{B}_{y,i-1/2,j+1/2} - \overline{B}_{y,i-1/2,j-1/2} - \overline{B}_{y,i+1/2,j-1/2}}{2\Delta y}, \tag{7}$$

then we have

$$\frac{\mathrm{d}}{\mathrm{d}t}(\nabla\cdot\mathbf{B})^U_{i,j} = \frac{1}{\Delta\tau^n}\left((\nabla\cdot\mathbf{B})^{V^n}_{i,j} - (\nabla\cdot\mathbf{B})^{U^n}_{i,j}\right). \tag{8}$$

Similarly, for the staggered V-cell, we have

$$\frac{\mathrm{d}}{\mathrm{d}t}(\nabla\cdot\mathbf{B})^V_{i+1/2,j+1/2} = \frac{1}{\Delta\tau^n}\left((\nabla\cdot\mathbf{B})^{U^n}_{i+1/2,j+1/2} - (\nabla\cdot\mathbf{B})^{V^n}_{i+1/2,j+1/2}\right). \tag{9}$$

It is easy to verify that $(\nabla\cdot\mathbf{B})^U_{i,j} = 0$ will be maintained if initially it is zero and $(\nabla\cdot\mathbf{B})^{V^n}_{i,j} = 0$ for every time step. Similar result has been obtained for the second-order staggered fully discrete schemes [1].

Remarks:

(1) In [7], a rigorous explanation is given as to why the cell-centered finite-volume methods fail to give stable results on the ideal MHD equations if the normal component of the magnetic field used in the flux calculation is discontinuous. However, the flux calculation for our central scheme on overlapping grid and the staggered fully discrete schemes of [1] is within the overlapping (or staggered) cell where the magnetic field is always continuous. This might be the reason why the central schemes of [2] and ours do not suffer from the instability described in [7].
(2) The semi-discrete formulation of [1] on a non-staggered grid does not have similar properties as (8). The authors in [1] claimed that $\nabla \cdot \mathbf{B} = 0$ is automatically preserved to machine round-off error, which is not true for general problems.
(3) The condition $(\nabla \cdot \mathbf{B})^{V^n}_{i,j} = 0$ is not easy to satisfy either. It involves nine V-cells and requires divergence-free reconstruction in each cell and the same reduced profile at a common face of two cells.
(4) If central schemes (2) and (3) are discretized by a third or higher order scheme, the divergence Eqs. (8) and (9) are no longer held for the numerical divergence (7). It is possible that a similar discrete conservation law to (8) is still held for a different discretization of $\nabla \cdot \mathbf{B}$.

2.4. Central schemes for the face-centered magnetic field

The constrained transport (CT) schemes are built upon area-averaged magnetic field components located at the faces of a grid cell, rather than volume-averaged field components located at grid cell centers. The need for a staggered grid is often thought of as a disadvantage of CT. However, the staggered grid is essential to conserve the magnetic flux, which is an area- rather than volume-averaged quantity in an integral sense.

The components of the area-averaged face-centered magnetic field are collocated at different faces. For a 2D example and cell $C_{i+1/2,j+1/2}$, the B_x component is defined as

$$\bar{b}^U_{x,i,j+1/2} = \frac{1}{\Delta y}\int_{y_j}^{y_{j+1}} B^U_x(x_i, y)\,\mathrm{d}y, \tag{10}$$

where the superscript U in B^U_x is used to differentiate the solution is for the U-cells or for the V-cells, the lower case b is used to indicate that this is a face-centered component of the magnetic field while the upper case B is used for the volume-averaged cell-centered component of the magnetic field. Analogue expressions can be written down for $\bar{b}^U_{y,i+1/2,j}$. The collocation of variables is illustrated in Fig. 2. The overlapping cells D_I provide more information for the collocated components of the magnetic field, since each face of the D_I is orthogonal to a face of $C_{I+1/2}$ at the face center. For a 2D problem, the location of the cell-centered magnetic field B of D_I is exactly the same location of the electric field E of $C_{I+1/2}$.

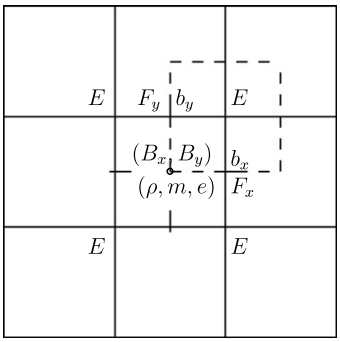

Fig. 2. Illustration of the staggered grid and the collocation of the magnetic field. The electrical field E is located at the cell corner. The magnetic field b_x and b_y, and flux F_x and F_y are located at the face center. The other fluid variables and cell-centered magnetic field B_x and B_y are located at the cell center.

In the following, we will describe how to derive the central schemes for the face-centered magnetic field using a 2D example. Applying schemes (2) and (3) directly to the induction Eq. (6), we obtain the central schemes for the face-centered magnetic field,

$$\frac{\mathrm{d}}{\mathrm{d}t}\bar{b}^{U}_{x,i,j+\frac{1}{2}}(t^n)=\frac{1}{\Delta\tau^n}\left(\frac{1}{\Delta y}\int_{y_j}^{y_{j+1}} b_x^{V^n}(x_i,y)\,\mathrm{d}y-\bar{b}^{U^n}_{x,i,j+\frac{1}{2}}\right)-\frac{E^V_{z,i,j+1}-E^V_{z,i,j}}{\Delta y}, \tag{11}$$

$$\frac{\mathrm{d}}{\mathrm{d}t}\bar{b}^{U}_{y,i+\frac{1}{2},j}(t^n)=\frac{1}{\Delta\tau^n}\left(\frac{1}{\Delta x}\int_{x_i}^{x_{i+1}} b_y^{V^n}(x,y_j)\,\mathrm{d}x-\bar{b}^{U^n}_{y,i+\frac{1}{2},j}\right)+\frac{E^V_{z,i+1,j}-E^V_{z,i,j}}{\Delta x}, \tag{12}$$

$$\frac{\mathrm{d}}{\mathrm{d}t}\bar{b}^{V}_{x,i+\frac{1}{2},j}(t^n)=\frac{1}{\Delta\tau^n}\left(\frac{1}{\Delta y}\int_{y_{j-\frac{1}{2}}}^{y_{j+\frac{1}{2}}} b_x^{U^n}(x_{i+\frac{1}{2}},y)\,\mathrm{d}y-\bar{b}^{V^n}_{x,i+\frac{1}{2},j}\right)-\frac{E^U_{z,i+\frac{1}{2},j+\frac{1}{2}}-E^U_{z,i+\frac{1}{2},j-\frac{1}{2}}}{\Delta y}, \tag{13}$$

$$\frac{\mathrm{d}}{\mathrm{d}t}\bar{b}^{V}_{y,i,j+\frac{1}{2}}(t^n)=\frac{1}{\Delta\tau^n}\left(\frac{1}{\Delta x}\int_{x_{i-\frac{1}{2}}}^{x_{i+\frac{1}{2}}} b_y^{U^n}(x,y_{i+\frac{1}{2}})\,\mathrm{d}x-\bar{b}^{V^n}_{y,i,j+\frac{1}{2}}\right)+\frac{E^U_{z,i+\frac{1}{2},j+\frac{1}{2}}-E^U_{z,i-\frac{1}{2},j+\frac{1}{2}}}{\Delta x}. \tag{14}$$

Note that the accuracy of the scheme depends only on the order of the reconstruction polynomial and the integral scheme.

To preserve the divergence-free condition, we require

$$\frac{\mathrm{d}}{\mathrm{d}t}\left((\bar{b}^U_{x,i+1,j+\frac{1}{2}}-\bar{b}^U_{x,i,j+\frac{1}{2}})\Delta y+(\bar{b}^U_{y,i+\frac{1}{2},j+1}-\bar{b}^U_{y,i+\frac{1}{2},j})\Delta x\right)(t^n)=0, \tag{15}$$

$$\frac{\mathrm{d}}{\mathrm{d}t}\left((\bar{b}^V_{x,i+\frac{1}{2},j}-\bar{b}^V_{x,i-\frac{1}{2},j})\Delta y+(\bar{b}^V_{y,i,j+\frac{1}{2}}-\bar{b}^V_{y,i,j-\frac{1}{2}})\Delta x\right)(t^n)=0. \tag{16}$$

Inserting Eqs. (11)–(14) into the above equations, and using the divergence-free condition at $t=t^n$, we obtain,

$$\int_{y_j}^{y_{j+1}} b_x^{V^n}(x_{i+1},y)\,\mathrm{d}y-\int_{y_j}^{y_{j+1}} b_x^{V^n}(x_i,y)\,\mathrm{d}y+\int_{x_i}^{x_{i+1}} b_y^{V^n}(x,y_{j+1})\,\mathrm{d}x-\int_{x_i}^{x_{i+1}} b_y^{V^n}(x,y_j)\,\mathrm{d}x=0 \tag{17}$$

$$\int_{y_{j-\frac{1}{2}}}^{y_{j+\frac{1}{2}}} b_x^{U^n}(x_{i+\frac{1}{2}},y)\,\mathrm{d}y-\int_{y_{j-\frac{1}{2}}}^{y_{j+\frac{1}{2}}} b_x^{U^n}(x_{i-\frac{1}{2}},y)\,\mathrm{d}y+\int_{x_{i-\frac{1}{2}}}^{x_{i+\frac{1}{2}}} b_y^{U^n}(x,y_{i+\frac{1}{2}})\,\mathrm{d}x-\int_{x_{i-\frac{1}{2}}}^{x_{i+\frac{1}{2}}} b_y^{U^n}(x,y_{i-\frac{1}{2}})\,\mathrm{d}x=0 \tag{18}$$

The evaluation of (17) involves four neighbor V-cells D_I, where

$$I=\{(x_i,y_j),\ (x_{i+1},y_j),\ (x_i,y_{j+1}),\ (x_{i+1},y_{i+1})\}.$$

To satisfy (17), we require the reconstruction polynomials on the four cells must satisfy the divergence-free condition internally and also have the same reduced polynomials along the common boundaries of the cells. Thus we must reconstruct at the cell boundaries first and then extend it to the whole cell. Similar conclusion is also held for condition (18).

3. Non-oscillatory hierarchical central reconstruction

The non-oscillatory hierarchical central reconstruction for the volume-averaged quantities has been described in Liu et al. [18]. In this section, we will focus on the non-oscillatory hierarchical central reconstruction for the face-centered magnetic field.

3.1. The third order divergence-free reconstruction over a cell

To achieve the high order accuracy, we must have a high order divergence-free reconstruction for the magnetic field. Balsara [4,5] has proposed a divergence-free TVD reconstruction. A similar second-order reconstruction was also proposed in [30]. For a 2D Cartesian grid, the parabolic reconstructed polynomials can be written as

$$B_x(x,y) = a_0 + a_x x + a_y y + \frac{1}{2}a_{xx}x^2 + a_{xy}xy + \frac{1}{2}a_{yy}y^2, \tag{19}$$

$$B_y(x,y) = b_0 + b_x x + b_y y + \frac{1}{2}b_{xx}x^2 + b_{xy}xy + \frac{1}{2}b_{yy}y^2. \tag{20}$$

To fit the linear profiles at the cell faces, Balsara [4] sets $a_{yy} = b_{xx} = 0$, which renders the polynomial to have only the second order accuracy.

To have the third order accuracy, we have to have a parabolic profile instead of the linear profile at the cell faces. For a 2D problem, we assume the magnetic field at the cell faces has the following form

$$B_x(x_i,y) = a_0^f(x_i) + a_y^f(x_i)y + \frac{1}{2}a_{yy}^f(x_i)y^2, \tag{21}$$

$$B_y(x,y_j) = b_0^f(y_j) + b_x^f(y_j)x + \frac{1}{2}b_{xx}^f(y_j)x^2, \tag{22}$$

where the superscript f denotes that the coefficient is for the face reconstruction. It is easy to find that Eqs. (19) and (20) cannot be matched to Eqs. (21) and (22) at the cell's four boundaries, even with the divergence-free condition. We then propose the following reconstructed polynomials

$$B_x(x,y) = a_0 + a_x x + a_y y + \frac{1}{2}a_{xx}x^2 + a_{xy}xy + \frac{1}{2}a_{yy}y^2 + \frac{1}{2}a_{xyy}xy^2 + \frac{1}{6}a_{xxx}x^3, \tag{23}$$

$$B_y(x,y) = b_0 + b_x x + b_y y + \frac{1}{2}b_{xx}x^2 + b_{xy}xy + \frac{1}{2}b_{yy}y^2 + \frac{1}{2}b_{xxy}x^2y + \frac{1}{6}b_{yyy}y^3, \tag{24}$$

which have total 16 coefficients. Imposing the divergence-free condition in a continuous sense gives five constraints on the coefficients,

$$a_x + b_y = 0; \quad a_{xx} + b_{xy} = 0; \quad a_{xy} + b_{yy} = 0; \quad a_{xyy} + b_{yyy} = 0; \quad a_{xxx} + b_{xxy} = 0. \tag{25}$$

Thus we have total 11 independent coefficients in the polynomials given by (23) and (24). The face profiles described by (21) and (22) have total 12 coefficients but only 11 of them are independent since the divergence-free condition must be satisfied. Integrating the magnetic fields along the boundaries of cell $C_{i+1/2,j+1/2} = [x_i, x_{i+1}] \times [y_j, y_{j+1}]$, we obtain $\nabla \cdot \mathbf{B} = 0$ as

$$\begin{aligned}&\left(a_0^f(x_{i+1}) + \frac{1}{24}(a_{yy}^f(x_{i+1}))(\Delta y)^2 - \left(a_0^f(x_i) + \frac{1}{24}(a_{yy}^f(x_i))(\Delta y)^2\right)\right)\Delta y \\ &+ \left(b_0^f(y_{j+1}) + \frac{1}{24}(b_{xx}^f(y_{j+1}))(\Delta x)^2 - \left(b_0^f(y_j) + \frac{1}{24}(b_{xx}^f(y_j))(\Delta x)^2\right)\right)\Delta x = 0\end{aligned} \tag{26}$$

Matching Eqs. (23) and (24) at the cell faces with Eqs. (21) and (22) gives the following solutions for the coefficients

$$a_y = \frac{a_y^{f_L} + a_y^{f_R}}{2} \tag{27}$$

$$a_{xy} = -b_{yy} = \frac{a_y^{f_R} - a_y^{f_L}}{\Delta x} \tag{28}$$

$$a_{yy} = \frac{a_{yy}^{f_L} + a_{yy}^{f_R}}{2} \tag{29}$$

$$a_{xyy} = -b_{yyy} = \frac{a_{yy}^{f_R} - a_{yy}^{f_L}}{\Delta x} \tag{30}$$

$$b_x = \frac{b_x^{f_B} + b_x^{f_T}}{2} \tag{31}$$

$$b_{xy} = -a_{xx} = \frac{b_x^{f_T} - b_x^{f_B}}{\Delta y} \tag{32}$$

$$b_{xx} = \frac{b_{xx}^{f_B} + b_{xx}^{f_T}}{2} \tag{33}$$

$$b_{xxy} = -a_{xxx} = \frac{b_{xx}^{f_T} - b_{xx}^{f_B}}{\Delta y} \tag{34}$$

$$a_0 = \frac{1}{2}\left(a_0^{f_L} + a_0^{f_R}\right) - \frac{1}{8}a_{xx}(\Delta x)^2 \tag{35}$$

$$b_0 = \frac{1}{2}\left(b_0^{f_B} + b_0^{f_T}\right) - \frac{1}{8}b_{yy}(\Delta y)^2 \tag{36}$$

$$a_x = \frac{a_0^{f_R} - a_0^{f_L}}{\Delta x} - \frac{1}{24}a_{xxx}(\Delta x)^2 \tag{37}$$

$$b_y = \frac{b_0^{f_T} - b_0^{f_B}}{\Delta y} - \frac{1}{24}b_{yyy}(\Delta y)^2 \tag{38}$$

where the subscripts L, R, T, B denote the values at the left, right, top, and bottom faces respectively for a specific cell. It can be easily verified that if the condition (26) is satisfied, a_x and b_y defined above satisfy $a_x + b_y = 0$.

Similarly we can obtain the fourth or higher order divergence-free reconstruction, which involves even more terms in (23) and (24).

3.2. TVD reconstruction at the face

As mentioned in the previous subsection, the divergence-free reconstruction over a cell is determined by the reconstruction at the four faces of the cell. In this subsection, we propose two approaches to construct a TVD parabolic profile for the face-centered magnetic field. Both reconstructions are for the CT method where the face-centered rather than the cell-centered magnetic fields are the primary variables. We will take B_x^U at the face $x = x_i$ of the cell $C_{i+1/2,j+1/2}$ as an example.

3.2.1. Parabolic reconstruction at the face using only a single grid information

The easiest way to construct a parabolic profile is to use three faces at $x = x_i$: $\bar{b}_x^U(x_i, y_{i+1/2})$ of the cell $C_{i+1/2,j+1/2}$, $\bar{b}_x^U(x_i, y_{j+3/2})$ of the cell $C_{i+1/2,j+3/2}$, and $\bar{b}_x^U(x_i, y_{j-1/2})$ of the cell $C_{i+1/2,j-1/2}$, all of which belong to a single grid U-cells. Integrating the parabolic profile $b_x = a_0^f(x_i, y_{j+\frac{1}{2}}) + a_y^f(x_i, y_{j+\frac{1}{2}})y + \frac{1}{2}a_{yy}^f(x_i, y_{j+\frac{1}{2}})y^2$ over the three faces, we have

$$\bar{b}_x^U(x_i, y_{i+\frac{1}{2}}) = a_0^f(x_i, y_{j+\frac{1}{2}}) + \frac{1}{24}a_{yy}^f(x_i, y_{j+\frac{1}{2}})(\Delta y)^2 \tag{39}$$

$$\bar{b}_x^U(x_i, y_{j-\frac{1}{2}}) = a_0^f(x_i, y_{j+\frac{1}{2}}) - a_y^f(x_i, y_{j+\frac{1}{2}})\Delta y + \frac{13}{24}a_{yy}^f(x_i, y_{j+\frac{1}{2}})(\Delta y)^2 \tag{40}$$

$$\bar{b}_x^U(x_i, y_{j+\frac{3}{2}}) = a_0^f(x_i, y_{j+\frac{1}{2}}) + a_y^f(x_i, y_{j+\frac{1}{2}})\Delta y + \frac{13}{24}a_{yy}^f(x_i, y_{j+\frac{1}{2}})(\Delta y)^2. \tag{41}$$

Solving the above equations, we obtain

$$a_y^f(x_i, y_{j+\frac{1}{2}}) = \frac{\bar{b}_x^U(x_i, y_{j+\frac{3}{2}}) - \bar{b}_x^U(x_i, y_{j-\frac{1}{2}})}{\Delta y}, \tag{42}$$

$$a_{yy}^f(x_i, y_{j+\frac{1}{2}}) = \frac{\bar{b}_x^U(x_i, y_{j+\frac{3}{2}}) - 2\bar{b}_x^U(x_i, y_{i+\frac{1}{2}}) + \bar{b}_x^U(x_i, y_{j-\frac{1}{2}})}{(\Delta y)^2}, \tag{43}$$

$$a_0^f(x_i, y_{j+\frac{1}{2}}) = \bar{b}_x^U(x_i, y_{i+\frac{1}{2}}) - \frac{1}{24}a_{yy}^f(x_i, y_{j+\frac{1}{2}})(\Delta y)^2. \tag{44}$$

We remark that our central parabolic reconstruction is quite different from the PPM (the piecewise-parabolic method; Woodward and Colella [31]). PPM constructs a parabola at the cell-interface using the 1D cell-average values. For example, for the cell average $\bar{f}_{i-2}$, $\bar{f}_{i-1}$, $\bar{f}_i$, and $\bar{f}_{i+1}$, the coefficients of the parabola are evaluated at $x = x_{i-1/2}$ and require four nearby cells.

3.2.2. Parabolic reconstruction at the face using the combined cells

The overlapping cells provide information to construct a more compact parabola. The difficulty lies in that the magnetic components of the V-cells are not collocated at the same position as the U-cells. To overcome this difficulty, we propose to construct a divergence-free polynomial over a virtual cell that fully contains one cell boundary.

Take B_x^U at face $x = x_i$ of the cell $C_{i+1/2,j+1/2}$ as an example (see the left plot of Fig. 3). We choose the virtual cell to be $[x_{i-1/2}, x_{i+1/2}] \times [y_j, y_{j+1}]$. We assume the polynomials over the virtual cell have the same form as Eqs. (19) and (20), but the coefficients are evaluated at the center $(x_i, y_{j+1/2})$ of the virtual cell. The parabola for the face $x = x_i$ will have the same form as Eq. (21).

As illustrated in Fig. 3, we will use the face-centered U-cell values $\bar{b}_x^U(x_i, y_{j+1/2})$, $\bar{b}_y^U(x_{i-1/2}, y_{j+1})$, $\bar{b}_y^U(x_{i+1/2}, y_{j+1})$, $\bar{b}_y^U(x_{i-1/2}, y_j)$, $\bar{b}_y^U(x_{i+1/2}, y_j)$, and face-centered V-cell values $\bar{b}_y^V(x_i, y_{j+1/2})$, $\bar{b}_x^V(x_{i-1/2}, y_{j+1})$, $\bar{b}_x^V(x_{i+1/2}, y_{j+1})$, $\bar{b}_x^V(x_{i-1/2}, y_j)$, $\bar{b}_x^V(x_{i+1/2}, y_j)$, plus the divergence-free condition to evaluate the coefficients of Eq. (19). After a complex manipulation, we obtain

$$a_y^f(x_i, y_{i+\frac{1}{2}}) = \frac{\tilde{b}_x(x_i, y_{j+1}) - \tilde{b}_x(x_i, y_j)}{\Delta y} \tag{45}$$

$$a_{yy}^f(x_i, y_{i+\frac{1}{2}}) = \frac{\tilde{b}_x(x_i, y_{j+1}) + \tilde{b}_x(x_i, y_j) - 2\bar{b}_x^U(x_i, y_{j+1/2})}{\left(\frac{1}{2}\Delta y\right)^2} - \frac{\Delta x}{(\Delta y)^3}\left(\bar{b}_y^U(x_{i+1/2}, y_{j+1}) + \bar{b}_y^U(x_{i-1/2}, y_j) - \bar{b}_y^U(x_{i-1/2}, y_{j+1}) - \bar{b}_y^U(x_{i+1/2}, y_j)\right) \tag{46}$$

$$a_0^f(x_i, y_{j+\frac{1}{2}}) = \bar{b}_x^U(x_i, y_{j+1/2}) - \frac{1}{24} a_{yy}^f(x_i, y_{j+\frac{1}{2}})(\Delta y)^2, \tag{47}$$

where $\tilde{b}_x(x_i, y_j) = \frac{1}{2}(\bar{b}_x^V(x_{i-1/2}, y_j) + \bar{b}_x^V(x_{i+1/2}, y_j))$. Similarly we can construct the parabola for the magnetic components B_y^U, B_x^V, and B_y^V.

Apparently the reconstruction (45)–(47) is more complicated than (42)–(44). However, by using the overlapping cells, the reconstruction (45)–(47) becomes more compact. This can be seen from the radius of the disk that covers the reconstruction stencil. The radius is $\sqrt{(\Delta x)^2 + (\Delta y)^2/4}$ for (45)–(47), and is $3\Delta y/2$ for (42)–(44). For a uniform grid with $\Delta x = \Delta y$, (45)–(47) is definitely more compact and hence will be less dissipative. This will be verified by the numerical examples in Section 4.

3.2.3. Non-oscillatory hierarchical reconstruction

The central reconstruction out of nearby cell averages generates polynomial in each cell. For solutions that contain discontinuities, Gibbs phenomenon could appear in the reconstructed polynomials. Liu et al. [18] pro-

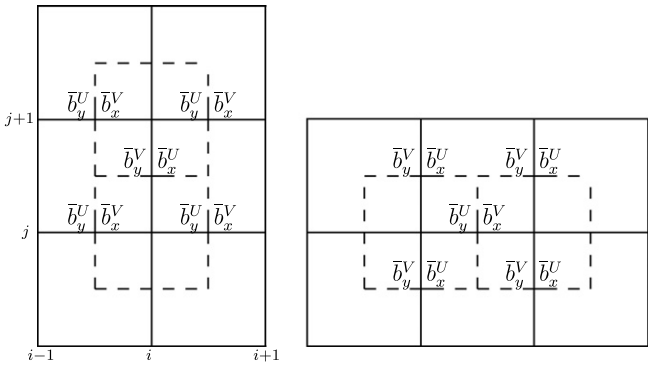

Fig. 3. The stencils used in parabolic reconstruction with the combined cell for the face-averaged magnetic fields. The dashed lines denote the boundaries of the V-cell, and the solid lines denote the boundaries of the U-cell. The left stencil is for the reconstruction of $\bar{b}_x^U$, and the right stencil is for the reconstruction of $\bar{b}_y^U$.

posed a non-oscillatory hierarchical reconstruction procedure to remove the possible oscillations and achieve high resolution near discontinuities.

To preserve the divergence-free condition $\nabla \cdot \mathbf{B} = 0$, we must perform the non-oscillatory limiting processing to the central reconstruction of the magnetic fields at the faces. Once we have a high order central reconstruction for the face-averaged magnetic field, e.g, (42)–(44) or (45)–(47), for every face, the application of the non-oscillatory hierarchical reconstruction is straightforward. Take the parabolic reconstruction Eq. (21) as an example. For the faces at $(x_i, y_{J+1/2})$, $J = j-1, j, j+1$, we have $b_x(x_i, y_{J+1/2}) = a_0^f(x_i, y_{J+1/2}) + a_y^f(x_i, y_{J+1/2})y + \frac{1}{2}a_{yy}^f(x_i, y_{J+1/2})y^2$. First we take the derivative with respect to y, which yields

$$L(x_i, y_{J+\frac{1}{2}}) = a_y^f(x_i, y_{J+\frac{1}{2}}) + a_{yy}^f(x_i, y_{J+\frac{1}{2}})y, \quad J = j-1, j, j+1. \tag{48}$$

Second, we calculate the face-average of $L(x_i, y_{J+1/2})$ on the face at $(x_i, y_{J+\frac{1}{2}})$ to obtain $\overline{L}(x_i, y_{J+1/2}) = a_y^f(x_i, y_{J+1/2})$. With the three new face averages $\{\overline{L}_J : J = j-1, j, j+1\}$, we can apply an essentially non-oscillatory (ENO) procedure to reconstruct a non-oscillatory linear polynomial

$$\widetilde{L}(x_i, y_{j+\frac{1}{2}}) = \tilde{a}_y^f(x_i, y_{j+\frac{1}{2}}) + \tilde{a}_{yy}^f(x_i, y_{j+\frac{1}{2}})y, \tag{49}$$

for the face at $(x_i, y_{j+1/2})$, where

$$\tilde{a}_{yy}^f = \mathrm{ENO}\left(\frac{\overline{L}(x_i, y_{j+\frac{1}{2}}) - \overline{L}(x_i, y_{j-\frac{1}{2}})}{\Delta y}, \frac{\overline{L}(x_i, y_{j+\frac{3}{2}}) - \overline{L}(x_i, y_{j+\frac{1}{2}})}{\Delta y}\right). \tag{50}$$

and

$$\mathrm{ENO}(c_1, c_2, \ldots, c_m) = c_j, \text{if} |c_j| = \min(|c_1|, |c_2|, \ldots, |c_m|). \tag{51}$$

Inserting $\tilde{a}_{yy}^f$ into the parabola, we then calculate the face averages for the linear part of the reconstruction

$$L_J(x_i) = \tilde{a}_0^f(x_i, y_{j+\frac{1}{2}}) + \tilde{a}_y^f(x_i, y_{j+\frac{1}{2}})(y - y_{j+\frac{1}{2}}), \tag{52}$$

on the three faces $J = j-1, j, j+1$, which yields

$$\overline{L}_J(x_i) = \bar{b}_{x,i,J+\frac{1}{2}} - \frac{1}{2}\tilde{a}_{yy}^f \int_{J-\frac{1}{2}}^{J+\frac{1}{2}} (y - y_{j+\frac{1}{2}})^2 \mathrm{d}y, \quad J = j-1, j, j+1. \tag{53}$$

where $\bar{b}_{x,i,J+\frac{1}{2}}$, $J = j-1, j, j+1$, are the face averages at the current time. We again apply an ENO procedure to evaluate $\tilde{a}_y^f$, which yields,

$$\tilde{a}_y^f = \mathrm{ENO}\left(\frac{\overline{L}_j(x_i) - \overline{L}_{j-1}(x_i)}{\Delta y}, \frac{\overline{L}_{j+1}(x_i) - \overline{L}_j(x_i)}{\Delta y}\right). \tag{54}$$

The ENO procedure can be replaced with an MUSCL procedure by a different limiter, such as minmod limiter, van Leer limiter, Woodward limiter, and super-bee limiter. To preserve the face-averaged value, we set

$$\tilde{a}_0^f = \bar{b}_{x,i,j+\frac{1}{2}} - \frac{1}{24}\tilde{a}_{yy}^f(\Delta y)^2. \tag{55}$$

Finally, we obtain the non-oscillatory reconstruction

$$\tilde{b}_x(x_i, y_{j+\frac{1}{2}}) = \tilde{a}_0^f + \tilde{a}_y^f(y - y_{j+\frac{1}{2}}) + \frac{1}{2}\tilde{a}_{yy}^f(y - y_{j+\frac{1}{2}})^2 \tag{56}$$

3.3. Volume-averaged cell-centered magnetic field

Unlike most of Godunov methods, the volume-averaged cell-centered magnetic field is rarely used in our central scheme using the face-centered magnetic field. In fact, the only case where the cell-centered magnetic field are used is in the time step prediction. The cell-centered magnetic field is obtained by

$$\overline{B}_x = a_0 + \frac{1}{24}(a_{xx}(\Delta x)^2 + a_{yy}(\Delta y)^2), \tag{57}$$

$$\overline{B}_y = b_0 + \frac{1}{24}(b_{xx}(\Delta x)^2 + b_{yy}(\Delta y)^2). \tag{58}$$

If we predict the time step during flux evaluation, the cell-centered magnetic field will not be used in the time evolution.

The pressure is only needed at the cell interface where the point-wise flux is calculated. It is derived from the internal energy density. The negative pressure is acceptable in our scheme though it is not physical. It usually occurs near a strong shock. Although the negative pressure will not break down the simulation, a fix can improve the overall pressure profile.

4. Numerical experiment

In this section, we provide some examples to test our third-order schemes with divergence-free reconstruction. To achieve the third-order in time, we apply the third-order TVD Runge-Kutta time integration (see [28]), which is

$$U^{(1)} = U^n + \Delta t R(U^n), \tag{59}$$

$$U^{(2)} = \frac{3}{4}U^n + \frac{1}{4}U^{(1)} + \frac{1}{4}\Delta t R(U^{(1)}), \tag{60}$$

$$U^{n+1} = \frac{1}{3}U^n + \frac{2}{3}U^{(2)} + \frac{2}{3}\Delta t R(U^{(2)}), \tag{61}$$

where $R(U)$ is the right-hand side of the ODE system obtained from un-split spatial discretization.

As pointed out in [18], the hierarchical reconstruction is expensive and takes about 30% of CPU time for our third-order scheme. As in [18], we use a low cost smoothness detector which measures the jump of the solution at the cell-center from reconstruction of neighbor cells. If the jump is smaller than $(\Delta x)^{3/2}$, the cell is considered to be in the smooth region and the hierarchical reconstruction procedure will not be performed. Usually the density and pressure are chosen as the candidate variables in the smoothness detector. For the face-centered magnetic field, our smoothness detector will detect the jump of the magnetic field at the face center. The ENO limiter (51) is used in all of the examples.

For comparison, we quantify the divergence of the magnetic field at a cell by integrating the reconstructed polynomials for B_x and B_y at the cell boundaries. For the parabolic reconstruction, it is approximated by

$$\nabla \cdot \mathbf{B} = a_x + b_y, \tag{62}$$

where a_x and b_y are the coefficients of the first-order terms in the reconstructed polynomial of B_x and B_y respectively.

The time step is determined by the CFL condition, which depends on the cell size and maximum signal speed over the whole domain. Without specification, the CFL number of 0.4 which is suggested in Liu et al. [18] is used. Unless specified otherwise, we will use $\gamma = 5/3$. For all the example, we show only the numerical results of the U-cells.

4.1. Smooth Alfvén wave problem

We first solve the smooth Alfvén wave problem [29] to check the accuracy of our proposed scheme. This problem describes propagation of a circularly polarized Alfvén wave in the domain $[0, 1/\cos\alpha] \times [0, 1/\sin\alpha]$ where α is the wave propagation angle relative to the x-axis. The initial conditions are taken as

$$\rho = 1, \quad v_{||} = 0, \quad v_\perp = 0.1\sin(2\pi\xi), \quad v_z = 0.1\cos(2\pi\xi)$$
$$p = 0.1, \quad B_{||} = 1, \quad B_\perp = v_\perp, \quad B_z = v_z$$

where $\xi = x\cos(\alpha) + y\sin(\alpha)$. In this problem, the Alfvén wave propagates periodically towards the origin with a constant Alfvén speed $B_{||}/\sqrt{\rho} = 1$ and returns to its initial state whenever t becomes an integer. In

Table 1
Numerical errors (δ_N) and convergence order (R_N) for the smooth Alfvén wave problem at $t = 2$ with and without CT

N	Non-CT		CT	
	δ_N	R_N	δ_N	R_N
16	0.0663255	–	0.0709366	–
32	0.0085469	2.96	0.0092040	2.95
64	0.0010724	2.99	0.0011562	2.99
128	0.0001341	3.00	0.0001446	3.00

our test, we use $\alpha = 45^\circ$. The domain is divided into $N \times N$ grid. As in [29], for each N, we estimate the relative numerical error of any fluid variable v by

$$\delta_N(v) = \frac{\sum_{j=1}^{N}\sum_{k=1}^{N}|v_{j,k}^{N} - v_{j,k}^{\text{exact}}|}{\sum_{j=1}^{N}\sum_{k=1}^{N}|v_{j,k}^{\text{exact}}|}, \tag{63}$$

Table 1 shows that average numerical errors defined by

$$\delta_N = \frac{1}{4}(\delta_N(v_\perp) + \delta_N(v_z) + \delta_N(B_\perp) + \delta_N(B_z)),$$

and the corresponding convergence orders, defined by $R_N = log(\delta_N/\delta_{N/2})/log(2)$, for both divergence-free constrained transport (CT) method and non-CT central schemes. For the CT method, we have also tested the two different face reconstructions described in Section 3, using or not using combined cells. The results are almost identical for this smooth problem and propagation angle. Therefore, we show only the results of using the combined cells in Table 1. The results show clearly that we have achieved the expected third-order accuracy for both CT and non-CT methods. The error of the CT method has only slight increase (<10%) over the error of the non-CT method, which is different from the results obtained by the second-order method proposed in Rossmanith [26], where the error for the CT method is more than double than the non-CT method.

4.2. Numerical dissipation and long term decay of Alfvén waves

Next we consider a problem proposed by Balsara [5], which tried to quantify the amount of numerical dissipation introduced by a numerical scheme for ideal MHD. Specifically, the test problem measures the decay of the amplitude of a linearly degenerate Alfvén wave that propagates at a shallow angle to the y-axis. We use the same angle, $\alpha = \tan(1/6) = 9.462^\circ$, and the same set of initial conditions as Balsara [5] except that the magnetic field is normalized with a $1/\sqrt{4\pi}$ factor. With the normalization, the B_z and v_z have the same exact solutions and thus have similar decay rates.

The computation domain is $[-3, 3] \times [-3, 3]$ on a 120×120 grid until time $t = 129$. The maximum values of the v_z and B_z should remain constant in time for the exact solution, but decay due to the numerical dissipation. These quantities are plotted versus time in Fig. 4. Since B_z and v_z have similar decay rates, we plot here only the result of v_z. For comparison, we have tested two different reconstructions described in Section 3, using or not using combined cells. Fig. 4 shows that the more compact reconstruction using the combined cells is less dissipative. We have tested the results of using $\Delta\tau^n$ and a smaller time step Δt^n in scheme (2) and (3). We set $\Delta\tau^n$ to be the value controlled by the CFL number, and $\Delta t^n = 0.1\Delta\tau^n$. Fig. 4 shows that we have achieved less dissipation using the smaller step than using $\Delta t^n = \Delta\tau^n$. Therefore our scheme is insensitive to small time step and can be applied to resistive MHD, which may require a smaller time step, without adding much numerical dissipation.

Fig. 4 shows that our third-order scheme is less dissipative than the "us,r=3WENO,HLL" (which refers to the unsplit solver with the fifth-order WENO reconstruction and HLLE-type Riemann solver) case of Balsara [5] but more dissipative than the "us,r=3WENO,Roe" case (see Fig. 4 of [5]). Note that "r=3WENO" of Balsara uses the fifth-order reconstruction while we use the third-order reconstruction.

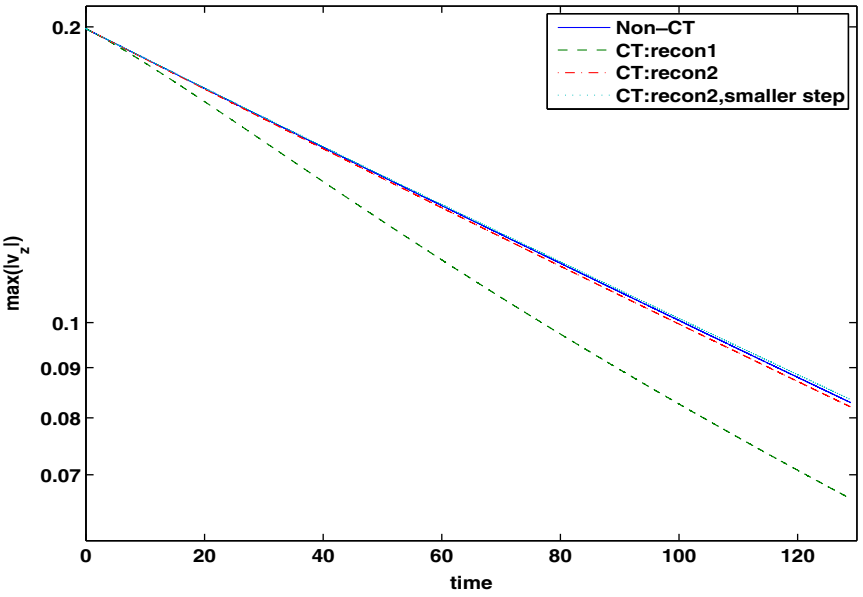

Fig. 4. Log-linear plot of the maximum value of z-component of the velocity. The maximum value should remain constant for the exact solution but decay due to the numerical dissipation. The "CT:reccon1" denotes the constrained transport (CT) with divergence-free reconstruction using (42)–(44). The "CT:reccon2" denotes the CT method with divergence-free reconstruction using (45)–(47), which uses the overlapping cell information and is more compact. The "CT:reccon2,smaller step" denotes "CT:reccon2" with the time integration using one-tenth of the regular time step.

4.3. Oblique shock tube problem

This shock-tube problem is originally from Brio and Wu [9], which is a classical test problem for ideal MHD codes. It is a 1-D shock-tube problem with the initial states

$$(\rho, v_{\|}, v_{\perp}, p, B_{\perp}, B_z, p) = \begin{cases} (1,0,0,0,1,0,1), & \text{left}, \\ (0.125,0,0,0,-1,0,0.1), & \text{right}, \end{cases}$$

where $\|$ refers to the direction along the normal of the shock front, $\perp$ refers to the direction perpendicular to the normal of the shock front but still in the computational plane, and $B_{\|} = 0.75$. We solve it as a fully 2-D problem with an angle $\alpha = 45^{\circ}$ between the shock interface and y-axes. The initial domain and grid set-up are similar to [29] with a shifted periodic boundary conditions. We use 400×4 grid to resolve a computational domain of $[0,1] \times [0,0.01]$. The Riemann solution for this example contains two fast shocks and two rarefaction waves, a slow compound, a contact discontinuity, and a slow shock (see Fig. 5 for the numerical results).

Unlike other Godunov schemes, the central scheme without CT performs very well for this shock tube problem. There is no noticeable difference between the results of CT and non-CT methods in the density and perpendicular component of the magnetic field ($B_{\perp} = -b_x \sin\alpha + by\cos\alpha$) plot. The divergence error without CT is also very small (see Fig. 6) and the parallel component ($B_{||} = b_x \cos\alpha + by \sin\alpha$) of the magnetic field is almost conserved. Note that the $B_{||} = 0.75$ is exactly conserved for the CT scheme.

4.4. Field loop advection

This is a problem proposed by Gardiner and Stone [12] to show the importance of maintaining divergence-free magnetic field during the time evolution. The computational domain is $[-1,1] \times [-0.5,0.5]$ and resolved by $2N \times N$ grid, and has periodic boundary conditions on both x- and y-boundaries. We adopt a similar set of initial conditions as [12], which is

$$\rho = 1, \quad p = 1, \quad v_x = 2, \quad v_y = 1, \quad v_z = 1, \quad B_z = 0.$$

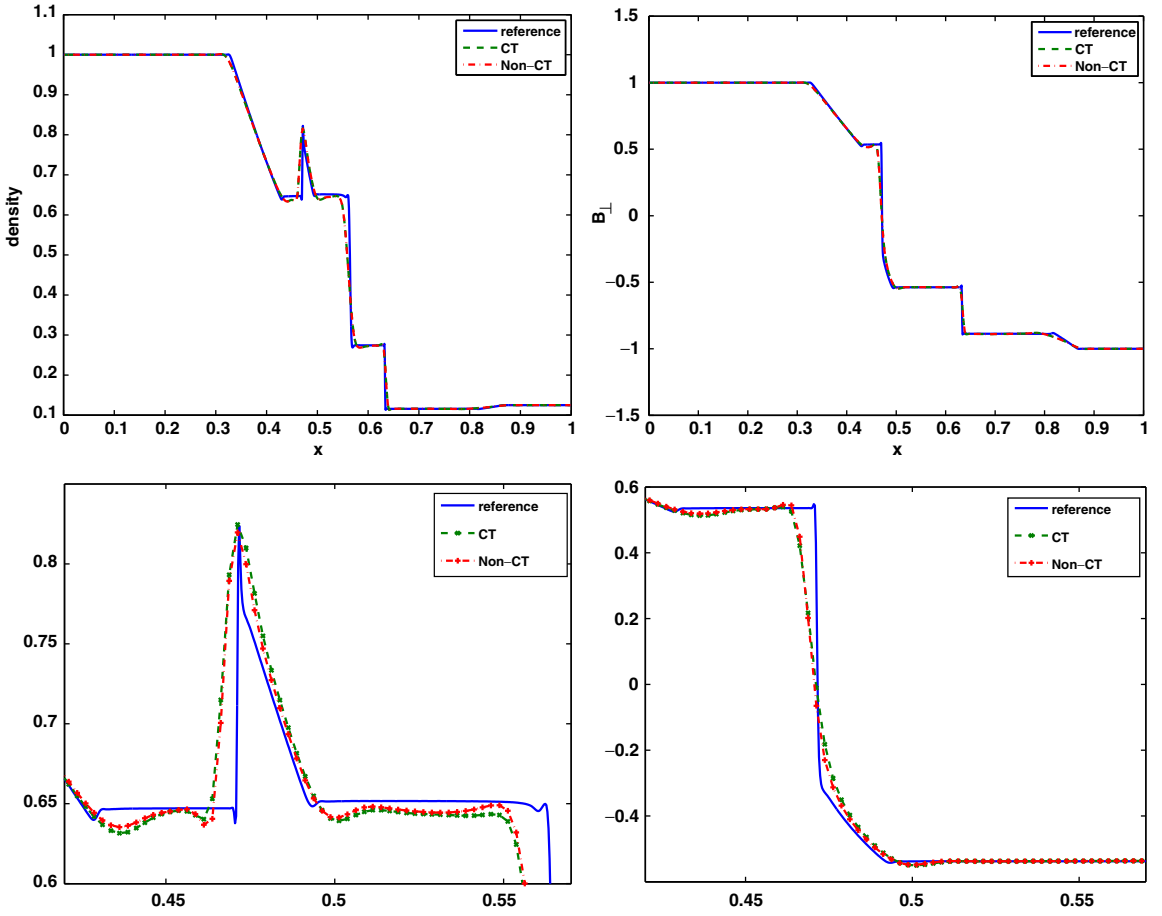

Fig. 5. The density (left) and the perpendicular component of the magnetic field (right) plot for the oblique shock tube problem with 400 grid cells and propagation angle $\alpha = 45°$. The bottom two are "zoomed" version of the top two for $x \in [0.42, 0.57]$. The output time is $t = 0.1/\sqrt{2}$. The reference solution is computed with 1600 grid cells in 1D problem ($\alpha = 0°$).

Note that we have set $v_z = 1$ to test whether B_z remains zero to round-off. The B_x and B_y components are initialized from the z-component of the magnetic potential

$$A_z = \begin{cases} A_0(R - r), & \text{if } r \leqslant R \\ 0 & \text{if } r > R \end{cases}$$

where $A_0 = 10^{-3}$, $R = 0.3$ and $r = \sqrt{x^2 + y^2}$. Since A_0 is so small, the magnetic field is essentially a passive scalar.

To our surprise, both CT and non-CT work well for this problem. Fig. 7 shows the magnetic field lines obtained by contouring the magnetic potential A_z at the beginning and at time $t = 2$. Since $\nabla \cdot \mathbf{B} \neq 0$ for the non-CT method, the magnetic potential is calculated approximately with the face-centered magnetic field defined by

$$b_{x,i,j+1/2} = \frac{1}{2}(B_{x,i+1/2,j+1/2} + B_{x,i-1/2,j+1/2}), \quad b_{y,i+1/2,j} = \frac{1}{2}(B_{y,i+1/2,j+1/2} + B_{x,i+1/2,j-1/2}).$$

The magnetic field lines for the non-CT scheme are slightly twisted due to the divergence error. Fig. 8 shows the dissipation of the magnetic energy as a function of time. The non-CT scheme is slightly less dissipative than the CT scheme. It is clear that the limiters play important role in the dissipation rate of the schemes. The CT scheme not only preserves the magnetic field lines better than the non-CT scheme, it also can preserve $B_z = 0$ to the round-off error (see the right plot of the Fig. 8).

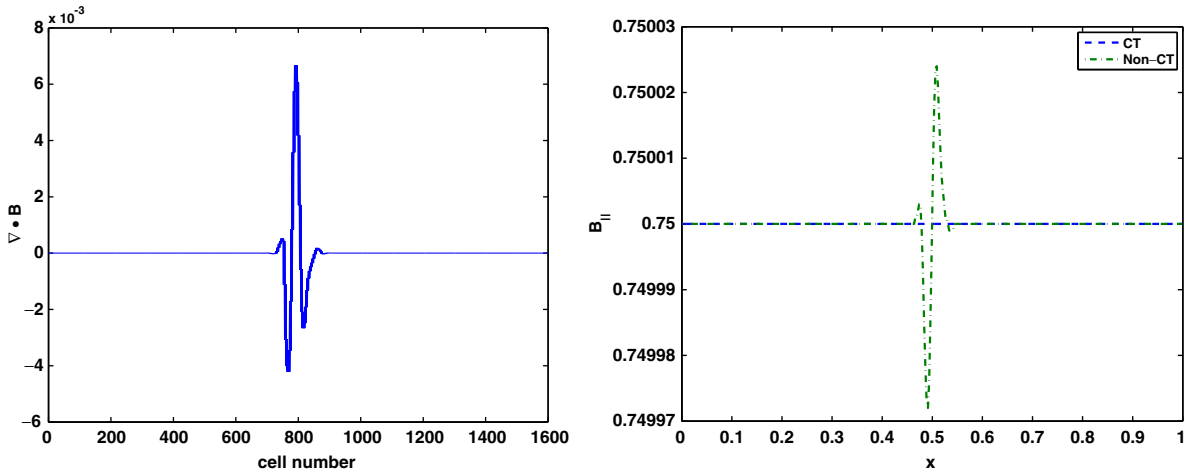

Fig. 6. The divergence error (left) and the parallel component of the magnetic field (right) plot for the oblique shock tube problem. $t = 0.1/\sqrt{2}$. The divergence error for the CT method is $O(10^{-13})$, which is not shown here. The CT method also preserves the parallel component of the magnetic field exactly.

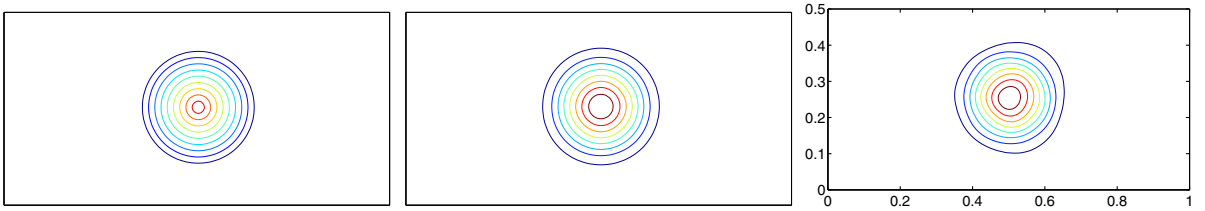

Fig. 7. Magnetic field lines at $t = 0$ (left) and $t = 2$ using CT (middle) and non-CT schemes (right) for the field loop advection problem. The uniform magnetic field lines are used for all of the three plots.

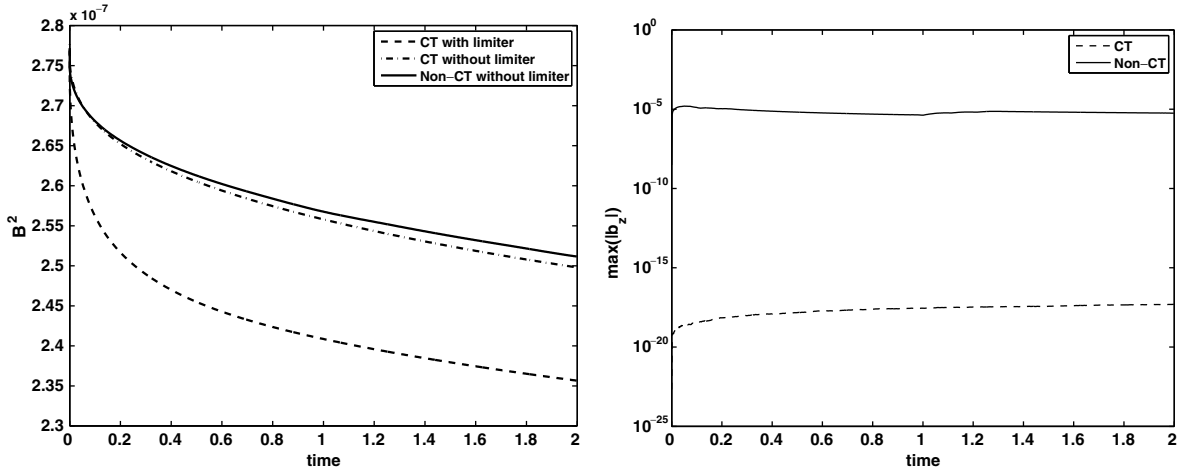

Fig. 8. The volume-averaged magnetic energy B^2 (left) and the maximum of B_z component (right) at a function of time for the field loop advection problem.

Most of high resolution shock-capturing (HRSC) schemes fail to solve this problem correctly without CT. To show the difference between our high-order central scheme on overlapping grid with the non-staggered central schemes in [1], we compare gray-scale images of the magnetic pressure $(B_x^2 + B_y^2)$ at $t = 0.15$ and $t = 2$. The

third-order schemes are tested. The magnetic field loop is passively advected around the grid with a period of 1. However, for the central scheme of [1] without CT, the field loop disintegrates before completing a fraction of an orbital period (see Fig. 9). Our third-order scheme without CT preserves the field loop quite well at $t = 0.15$, but not as well as with CT at $t = 2$. The divergence error plays an important role in disintegrating the field loop. Fig. 10 shows the divergence error of the magnetic fields for central scheme of [1] on non-staggered grid and the our central scheme on overlapping grid. It is clear that our scheme has much smaller divergence error than that of [1].

4.5. Current sheet

This is a test problem also suggested by Gardiner and Stone [12] to discriminate between algorithms and test the numerical dissipation and robustness of the integration algorithm.

The computational domain, $[0,1] \times [0,1]$, is resolved by 200×200 grid and has periodic boundary conditions on both x- and y-boundaries. The initial condition is

$$\rho = 1, \quad p = 0.1, \quad v_x = v_0 \sin(2\pi y), \quad v_y = v_z = 0, \quad B_x = B_z = 0,$$

and

$$B_y = \begin{cases} B_0 & \text{if } 0 \leqslant x < \frac{1}{4} \\ -B_0 & \text{if } \frac{1}{4} \leqslant x \leqslant \frac{3}{4} \\ B_0 & \text{if } x > \frac{3}{4} \end{cases} \tag{64}$$

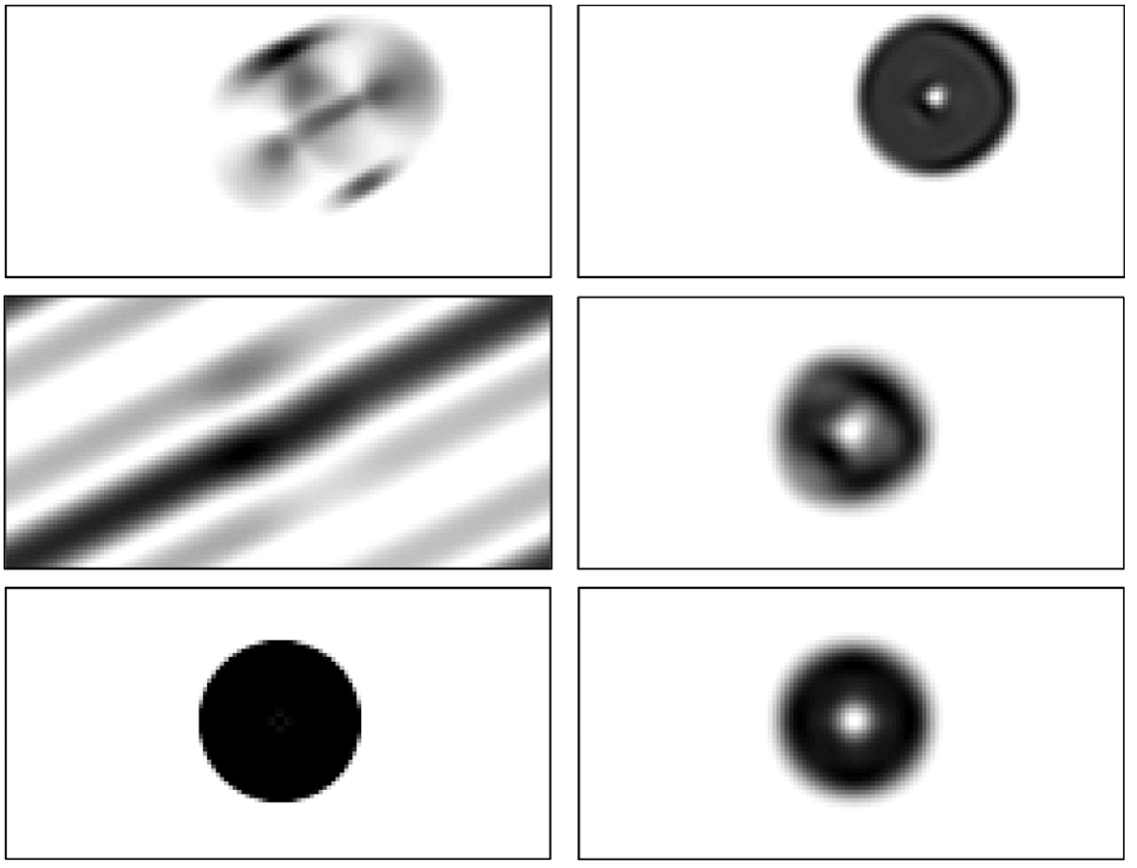

Fig. 9. Gray-scale images of the magnetic pressure $(B_x^2 + B_y^2)$ at $t = 0.15$ (top two) and $t = 2$ (middle two) without CT for the field loop advection problem. The left two are for the non-staggered central schemes of [1]. The right two are for our central schemes on overlapping grid. The bottom two are the reference solutions for the initial field loop at $t = 0$ and the CT results at $t = 2$. The emergence of a hole at the center is caused by reconnection.

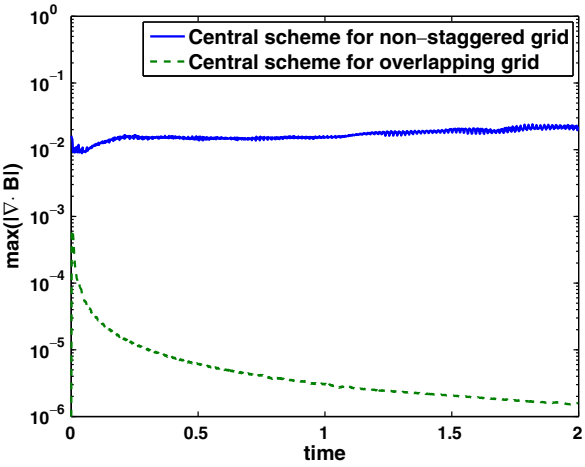

Fig. 10. Divergence error of the magnetic field for the non-CT central schemes on non-staggered grid (see [1]) and on overlapping grid.

where $B_0 = 1$, and $v_0 = 0.1$. Gardiner and Stone [12] provides a detailed physical description of this problem. To make the problem more difficult to solve, we set $v_0 = 2.0$, and $p = 0.05$.

Fig. 11 shows the magnetic field lines at different times. The magnetic potential for the non-CT schemes is calculated approximately in the same way as for the field-loop example. Because of the two current sheets in the problem (at $x = 0.25$ and $x = 0.75$), reconnection inevitably occurs. As reconnection takes place, the magnetic energy is converted into thermal energy. Because $\beta = 2p/\mathbf{B}^2 < 1$, the reconnection drives strong overpressured regions that launch magneto-sonic waves transverse to the field. Moreover, as reconnection changes the topology of the field lines, magnetic islands will form, grow, and merge. Since the nonlinear dynamics lead to strong compressions and rarefactions, it is important to make sure that the algorithm can follow this evo-

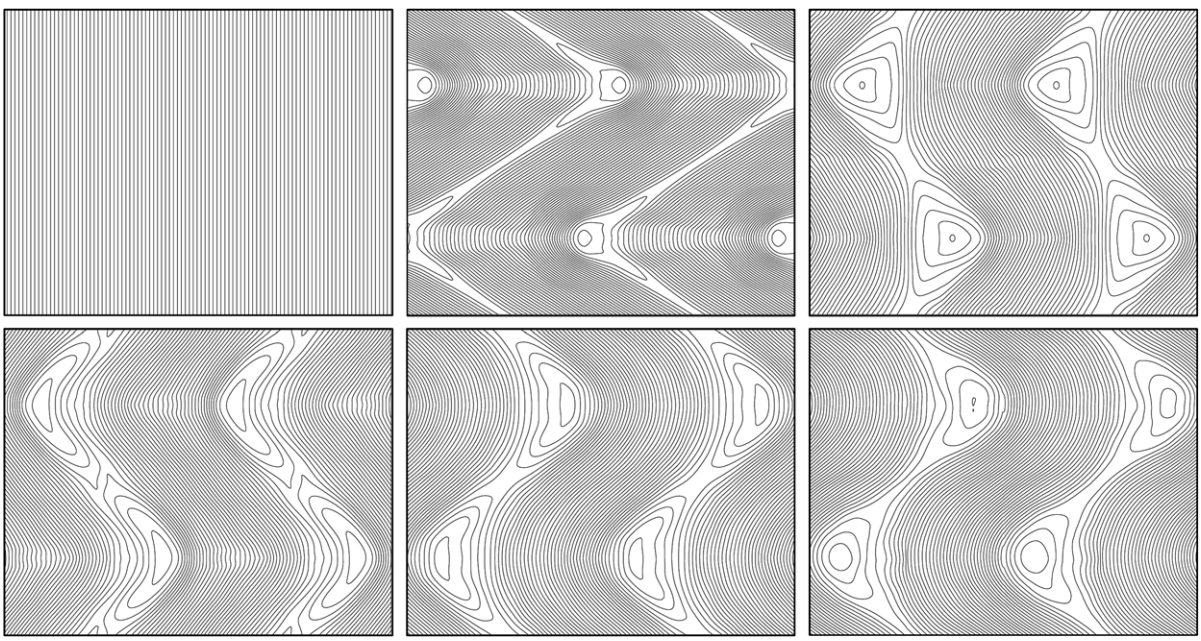

Fig. 11. Time evolution of the magnetic field lines for the current sheet problem. Time increases from left to right and top to bottom in normal reading order. The plotted contour levels of A_z (50 levels) are uniform over the sequences of images at time $t = (0.0, 1.0, 2.0, 3.0, 4.0, 4.0)$. The last plot is for non-CT method.

lution for as long as possible without crashing. By either increasing v_0 or decreasing p (and therefore β), the dynamics becomes increasing difficult for the numerical algorithm to solve. For our implementation of the third-order central scheme with and without CT, the code crashes at late times when $\beta \leqslant 0.001$ (for $v_0 = 0.1$), and when $v_0 \geqslant 9$ (for $\beta = 0.1$).

Fig. 12 shows the divergence error comparison between the CT and non-CT methods. Again the divergence-error for the non-CT method is quite small.

For a quantitative comparison of the various schemes, we calculate the relative numerical error as in [29]. In the absence of the exact solution, a high resolution numerical solution is used as a reference for comparison. For this example, the reference solution is calculated using 400×400 cells. The relative numerical error of variable v obtained on an $N \times N$ grid is defined as

$$\delta_N(v) = \frac{\sum_{j=1}^{N}\sum_{k=1}^{M}|v_{j,k}^{N} - v_{j,k}^{\text{high}}|}{\sum_{j=1}^{N}\sum_{k=1}^{N}|v_{j,k}^{\text{high}}|}, \tag{65}$$

where v^{high} is the coarsened high resolution solution. The numerical error is measured for the primitive variables. The averaged error $\bar{\delta}_N$ is defined as an averaged $\delta_N(v)$ for all the (non-zero) primitive variables v. Table 2 lists the average relative errors for the primitive variables for three resolutions (50×50, 100×100, and 200×200). For this discontinuity dominant flow, the convergence rate is around 1.0.

4.6. The blast problem

This test problem was first introduced in Balsara and Spicer [3]. It was about a spherical strong fast magneto-sonic shock propagates through a low-β ($\beta = 0.000251$) ambient plasma. It was used in [5] to show the advantages of the divergence-free reconstruction. The set-up of the problem is exactly the same as was described in [3]: $\rho = 1$, $\mathbf{v} = 0$, $B_x = 100/\sqrt{4\pi}$, $B_y = B_z = 0$, $p = 1000$ within a circle of radius $R = 0.1$ and

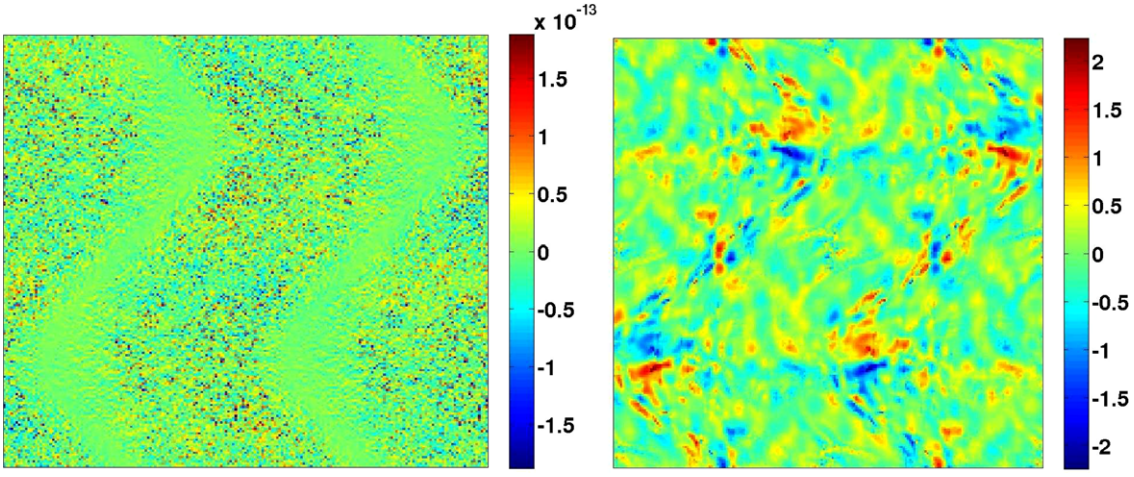

Fig. 12. Divergence of the magnetic field at $t = 4$ using CT (left) and non-CT (right) method for the current sheet problem.

Table 2
Convergence of averaged errors in the current-sheet test

	$t = 1.0$			$t = 4.0$		
	$\bar{\delta}_{50}$	$\bar{\delta}_{100}$	$\bar{\delta}_{200}$	$\bar{\delta}_{50}$	$\bar{\delta}_{100}$	$\bar{\delta}_{200}$
CT	0.2204	0.1168	0.0507	0.4173	0.1656	0.0956
Non-CT	0.2259	0.1129	0.0604	0.4332	0.1816	0.0998

$p = 0.1$ elsewhere. 200×200 grid with outflow boundary conditions is used. The final time is 0.01. The density contour plots both CT and non-CT methods are shown in Fig. 13. We also show the divergence error of the magnetic field in Fig. 14.

As pointed out by Balsara [5], this is a very stringent problem to solve with the parameters we have used. Our second-order Godunov method (see [16]) cannot work without the energy-fix defined in [3]. However, our constrained transport third-order central scheme on overlapping cells does not fail without the energy fix. We remark that the pressure can become negative near the shock front using our method (see Fig. 15). However, the negative pressure does not break down our integration. Using a more diffusive limiter combined with negative pressure fix can slightly improve the solutions (see Fig. 16), especially the pressure profile.

4.7. Rotor problem

This test problem is taken from Ref. [3]. It was also used by Tóth [29] to compare several numerical schemes. We use exactly the same set-up of the problem as was described in [29].

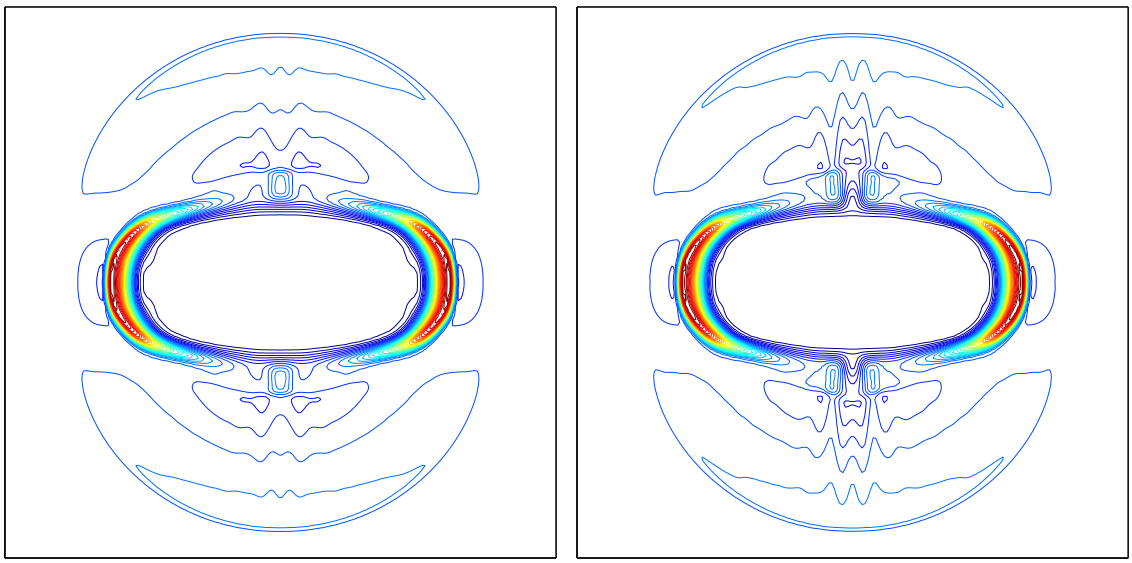

Fig. 13. Density contour plot using CT (left) and non-CT (right) method at $t = 0.01$ for the MHD blast problem. 40 contour-lines between 0.2 and 4.45 are used.

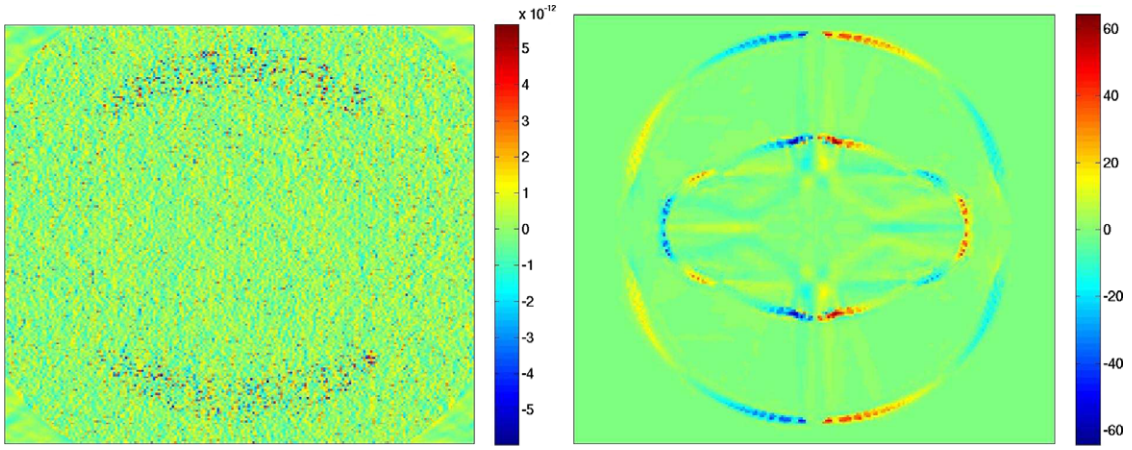

Fig. 14. Divergence of the magnetic field at $t = 0.01$ using CT (left) and non-CT (right) method for the MHD blast problem.

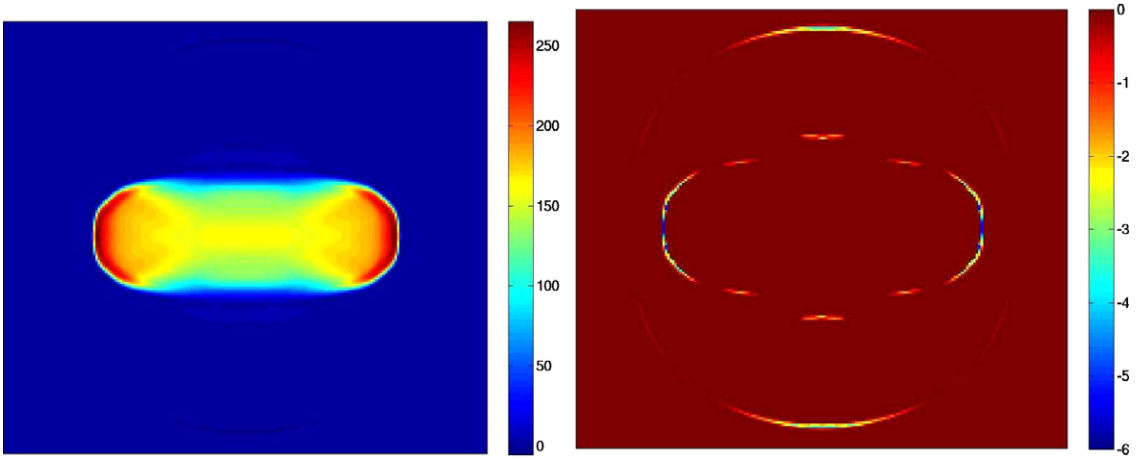

Fig. 15. Overall pressure plot (left) and the negative pressure region (right) at $t = 0.01$ for the MHD blast problem.

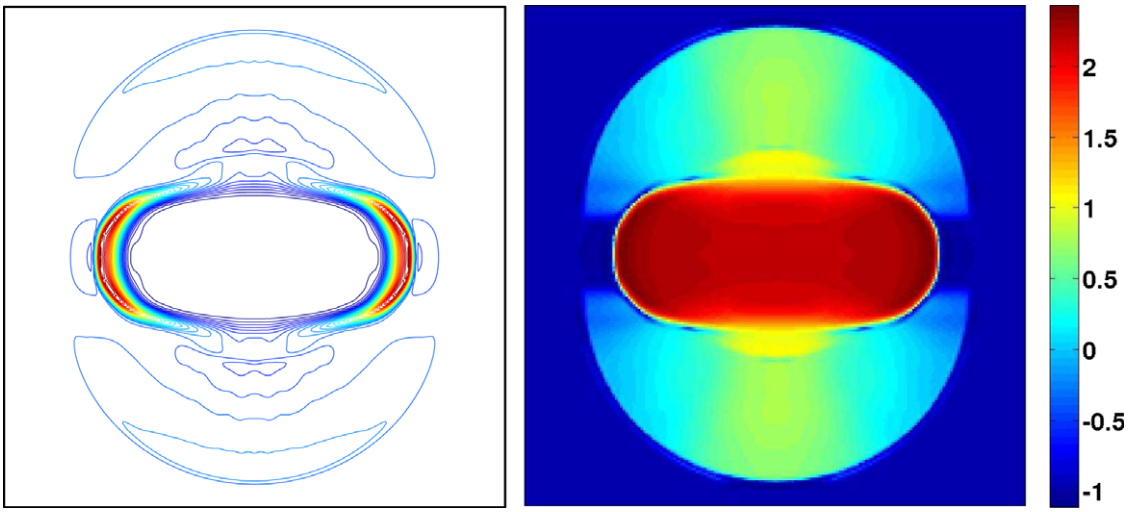

Fig. 16. Density contour plot (left) and logscale (base 10) plot of the pressure (right) using CT after pressure fix at $t = 0.01$ for the MHD blast problem. 40 contour-lines between 0.2 to 4.45 are used.

We solve the first rotor problem of Ref. [29] to time 0.15. A disk radius $R = 0.1$ made up of dense fluid ($\rho = 10$) rotates with a high angular velocity ($\omega = 20$) in a static, magnetized ($B_x = 5$) background with uniform density and pressure ($\rho = p = 1$). The adiabatic index is $\gamma = 1.4$. It was reported by Tóth [29] that many one step TVD base scheme failed to solve this problem due to negative pressure. We did not encounter any difficulties using our central scheme on overlapping cells with and without CT. Londrillo and Del Zanna [22] reported that the Balsara and Spicer's flux-CT approach produces a lot of numerical noise inside the disk, which is also seen in Toth's plot ([29]). However, we have not seen such kind of noises even in the results of our central scheme without CT (see Fig. 17). Fig. 18 shows the divergence-error in the entire domain.

4.8. Orszag–Tang vortex

The problem has becomes a standard test problem for 2D numerical MHD simulations (e.g. [10,14,21]). The initial conditions are $v_x = -\sin(y)$, $v_y = \sin(x)$, $B_x = -\sin(y)$, $B_y = \sin(2x)$, $\rho = \gamma^2$, $p = \gamma$, $v_z = B_z = 0$. The computational domain is a square $[0, 2\pi] \times [0, 2\pi]$ with periodic boundary conditions along both boundaries. The final output time $t = \pi$.

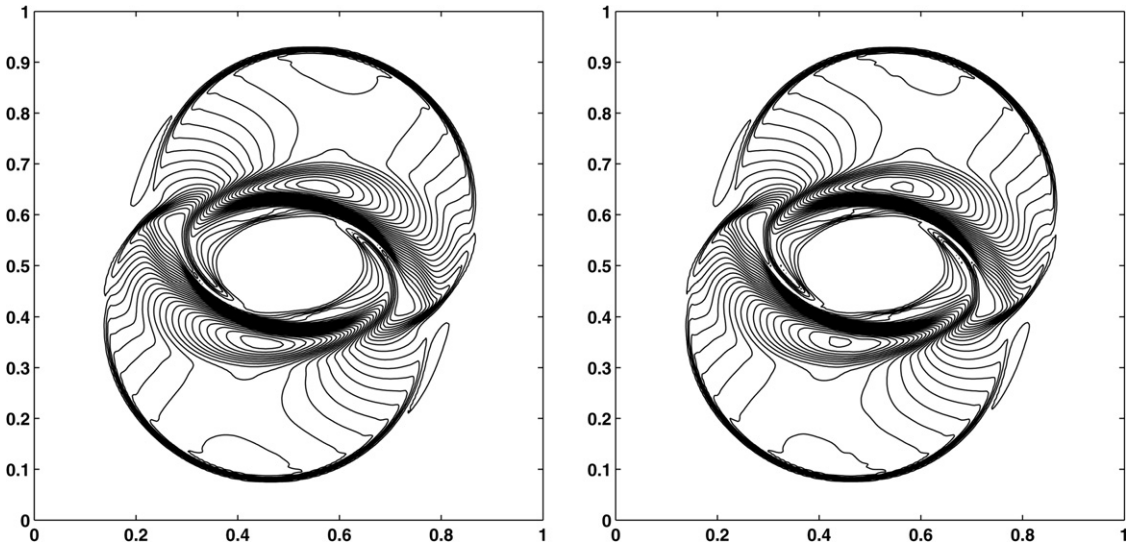

Fig. 17. Contour plot of the magnetic pressure ($B^2/2$) distribution with CT (left) and without CT (right) at $t = 0.15$ for the rotor problem. 31 contour-lines between 0.0787 and 2.5315 are used.

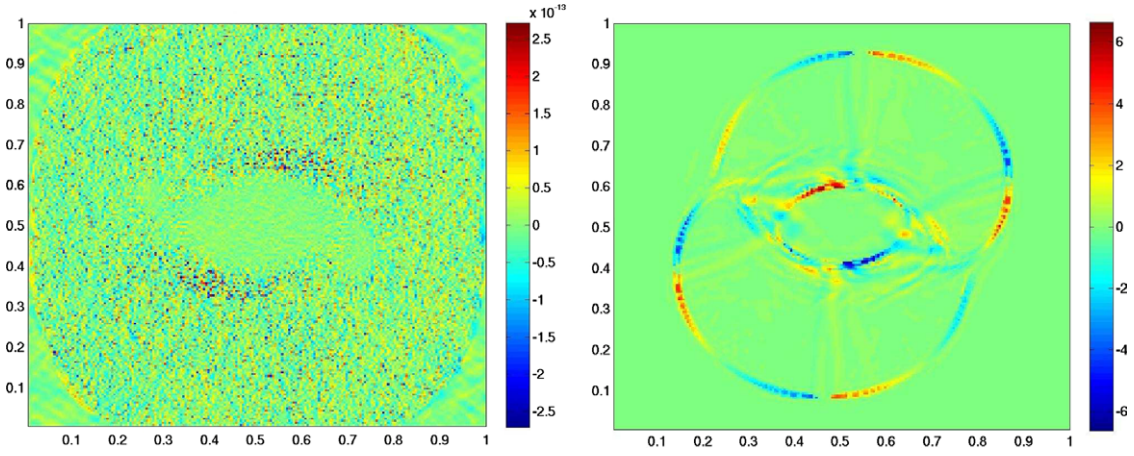

Fig. 18. Divergence error distribution of the magnetic field with CT (left) and without CT (right) at $t = 0.15$ for the rotor problem.

Fig.19 shows a Schlieren plot of the thermal pressure at time $t = \pi$ using our third-order CT central scheme on overlapping cells on a 256×256 grid. A slice of this solution at $y = 1.9267$ is also shown in Fig. 19. Our results compare well with those given in [10,26,29].

As discussed in [26], we also compare the solutions at $t = 0.633$ with and without CT. Fig. 20 shows that our method without CT does not produce negative pressure throughout the simulations. The solutions with and without CT are almost identical. Our divergence errors at final time are also much smaller than those shown in [26]. At least for this problem we have not seen noticeable difference between CT and non-CT methods.

The Orszag–Tang vortex problem starts from smooth initial condition data, but gradually the flow becomes very complex as expected from a transition towards turbulence. Table 3 lists the average relative errors for the primitive variables for three resolutions (64×64, 128×128, and 256×256). The reference solution is calculated with 512×512 grid. At time $T = 0.633$, the flow is still quite smooth, although some discontinuities are

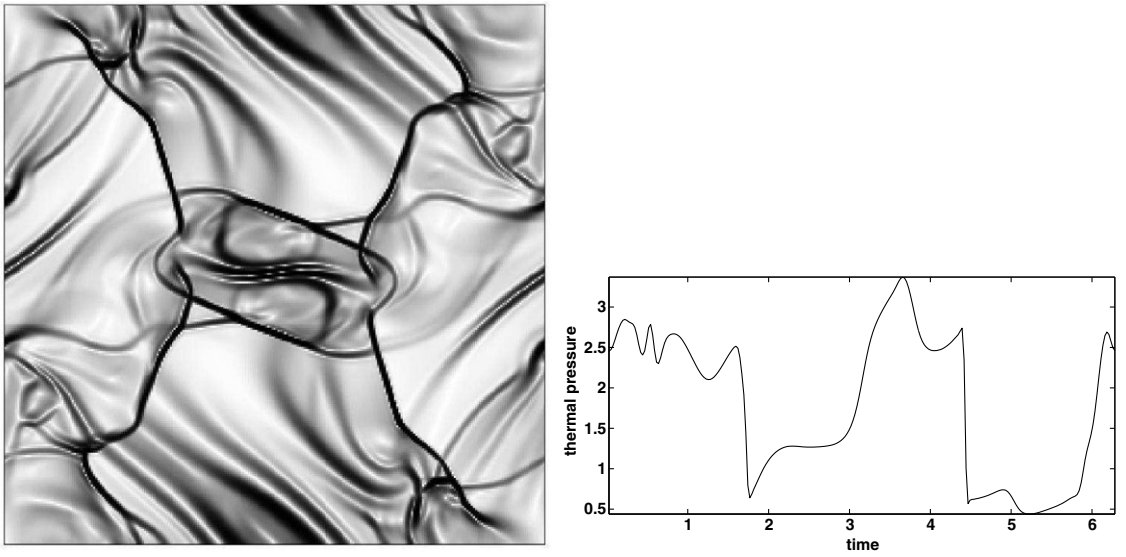

Fig. 19. The thermal pressure at $t = \pi$ for the Orszag–Tang vortex problem. Shown are a Schlieren plot over the entire domain (left) and a horizontal slice at $y = 1.9267$ (right). CT is used.

already present. The CT scheme converges with a convergence rate of approximate 2.7, and the non-CT scheme converges with a rate of approximate 2.15. Both rates are better than the first order accuracy obtained in dominantly discontinuous problems, but worse than the third-order accuracy expected for completely smooth flow.

5. Conclusion

We have applied the central scheme on overlapping cells to the MHD simulations. We have proposed a third-order divergence-free reconstruction and corresponding third-order CT scheme to preserve the divergence-free condition for the magnetic field throughout the simulation. Numerical examples show we have truly achieved the expected third-order accuracy for smooth problems. Our third-order divergence-free reconstruction can also be applied to non-staggered grid. Our approach can also be extended to construct higher than the third-order schemes without difficulty.

The overlapping cells provide a natural way to evaluate the electric field at the staggered points for the CT scheme without spatial averaging. The two-dimensional CT scheme based on this reduces exactly to the base one-dimensional algorithm for planar grid-aligned flows. Even though using the overlapping cells is more expensive, Liu et al. [18] show it is more robust without characteristic decomposition for higher order reconstructions. Our experience also shows that the central scheme on the overlapping cells achieves more accurate and higher resolution results than the corresponding central scheme on the non-staggered grid. A potential weakness is in its extension to the adaptive mesh refinement (AMR) grid.

Several numerical examples show that the high order central scheme on overlapping cells without CT has extremely good properties in maintaining low divergence-error, even for strong shock problem. It also has less numerical dissipation than with CT due to a more compact stencil used. We also observe that adding CT will increase the computational cost by 30%. We have yet to find example to show that the CT results are much more superior than without CT.

While the algorithm presented in this paper has focused solely on the two-dimensional case, the results presented here can be extended to three dimensions. This extension principally involves a more complex high order divergence-free reconstruction (see Appendix A) and high order quadrature rule on the surfaces and edges. The other details of this extension are beyond the scope of this paper and will be presented elsewhere.

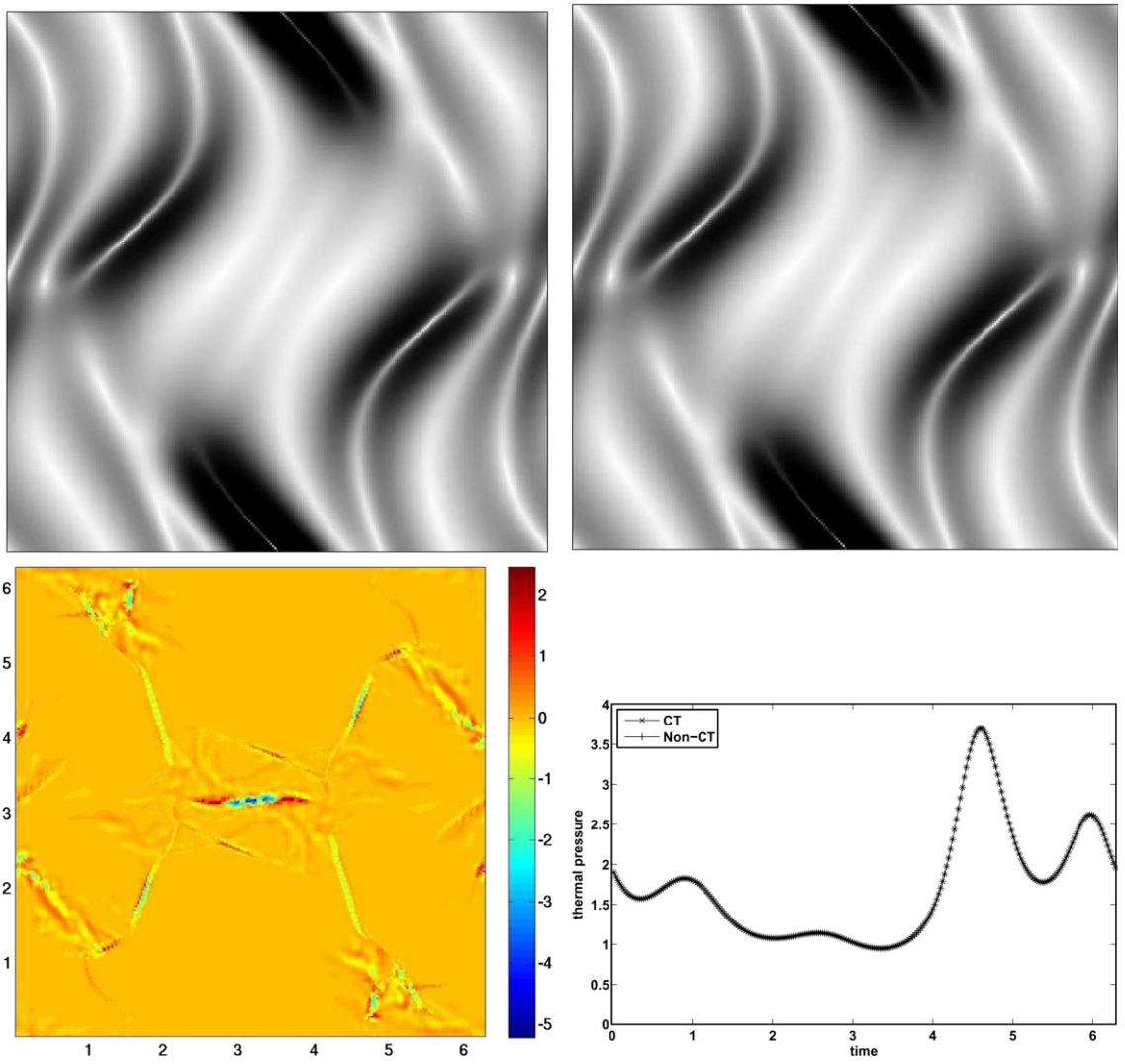

Fig. 20. The thermal pressure at $t = 0.633$ for the Orszag–Tang vortex problem. The top two show Schlieren plots over the entire domain with CT (left) and without CT (right). The bottom left shows the divergence error over the entire domain without CT at final time $t = \pi$. The bottom right shows a horizontal slice at $y = 2.3439$ for both with CT and without CT at time $t = 0.633$.

Table 3
Convergence of averaged errors in the Orszag–Tang test

	$t = 0.633$			$t = 3.14$		
	$\bar{\delta}_{64}$	$\bar{\delta}_{128}$	$\bar{\delta}_{256}$	$\bar{\delta}_{64}$	$\bar{\delta}_{128}$	$\bar{\delta}_{256}$
CT	2.347E-3	3.807E-4	5.552E-5	8.025E-2	4.013E-2	1.612E-2
Non-CT	3.394E-3	7.552E-4	1.722E-4	7.877E-2	3.956E-2	1.657E-2

Acknowledgements

We would like to thank Dr. Y. Liu for providing his code for the hydrodynamics. We also thank referees for many useful comments. This research was performed under the auspices of the Department of Energy. It was supported by the Laboratory Directed Research and Development (LDRD) Program at Los Alamos.

Appendix A. The third order divergence-free reconstruction in 3D

In 3D, the parabolic profile on the 2D surface of a cell can be written as

$$B_x(y,z) = a_0^f + a_y^f y + a_z^f z + \frac{1}{2}a_{yy}^f y^2 + a_{yz}^f yz + \frac{1}{2}a_{zz}^f z^2, \tag{A.1}$$

$$B_y(x,z) = b_0^f + b_x^f x + b_z^f z + \frac{1}{2}b_{xx}^f x^2 + b_{xz}^f xz + \frac{1}{2}b_{zz}^f z^2, \tag{A.2}$$

$$B_z(x,y) = c_0^f + c_x^f x + c_y^f y + \frac{1}{2}c_{xx}^f x^2 + c_{xy}^f xy + \frac{1}{2}c_{yy}^f y^2, \tag{A.3}$$

where again the superscript ^{f} denotes that the coefficient is for the face reconstruction. The reconstructed field in the interior of the cell that matches the parabolic profile on the cell faces can be written as

$$\begin{aligned} B_x(x,y,z) = {} & a_0 + a_x x + a_y y + a_z z + \frac{1}{2}a_{xx}x^2 + a_{xy}xy + a_{xz}xz + \frac{1}{2}a_{yy}y^2 + a_{yz}yz \\ & + \frac{1}{2}a_{zz}z^2 + \frac{1}{6}a_{xxx}x^3 + \frac{1}{2}a_{xxy}x^2y + \frac{1}{2}a_{xxz}x^2z + \frac{1}{2}a_{xyy}xy^2 + a_{xyz}xyz + \frac{1}{2}a_{xzz}xz^2, \end{aligned} \tag{A.4}$$

$$\begin{aligned} B_y(x,y,z) = {} & b_0 + b_x x + b_y y + b_z z + \frac{1}{2}b_{xx}x^2 + b_{xy}xy + b_{xz}xz + \frac{1}{2}b_{yy}y^2 + b_{yz}yz \\ & + \frac{1}{2}b_{zz}z^2 + \frac{1}{2}b_{xxy}x^2y + \frac{1}{2}b_{xyy}xy^2 + b_{xyz}xyz + \frac{1}{6}b_{yyy}y^3 + \frac{1}{2}b_{yyz}y^2z + \frac{1}{2}b_{yzz}yz^2, \end{aligned} \tag{A.5}$$

$$\begin{aligned} B_z(x,y,z) = {} & c_0 + c_x x + c_y y + c_z z + \frac{1}{2}c_{xx}x^2 + c_{xy}xy + c_{xz}xz + \frac{1}{2}c_{yy}y^2 + c_{yz}yz \\ & + \frac{1}{2}c_{zz}z^2 + \frac{1}{2}c_{xxz}x^2z + c_{xyz}xyz + \frac{1}{2}c_{xzz}xz^2 + \frac{1}{2}c_{yyz}y^2z + \frac{1}{2}c_{yzz}yz^2 + \frac{1}{6}c_{zzz}z^3. \end{aligned} \tag{A.6}$$

Imposing the divergence-free condition in a continuous sense gives ten constraints on the coefficients,

$$\begin{aligned} & a_x + b_y + c_z = 0, \quad a_{xx} + b_{xy} + c_{xz} = 0, \\ & a_{xy} + b_{yy} + c_{yz} = 0, \quad a_{xz} + b_{yz} + c_{zz} = 0, \\ & a_{xxx} + b_{xxy} + c_{xxz} = 0, \quad a_{xyy} + b_{yyy} + c_{yyz} = 0, \\ & a_{xzz} + b_{yzz} + c_{zzz} = 0, \quad a_{xxy} + b_{xyy} + c_{xyz} = 0, \\ & a_{xxz} + b_{xyz} + c_{xzz} = 0, \quad a_{xyz} + b_{yyz} + c_{yzz} = 0. \end{aligned} \tag{A.7}$$

Note that we have total of 48 coefficients in Eqs. (A.4)–(A.6) and have ten constraints. Thus we have only 38 independent coefficients. However the face profiles described by (A.1)–(A.3) are described by only 35 independent numbers if the divergence-free condition must be satisfied. The system of equations is under-determined. Since we focus on the third-order reconstruction, the third-order terms in the polynomials can be arbitrary once they satisfy the divergence-free constraints (A.7). Following Balsara [4], we make simplifying choices for three of the polynomial coefficients and set

$$b_{yyz} = c_{yzz}, \quad a_{xxz} = c_{xzz}, \quad a_{xxy} = b_{xyy}.$$

Then the polynomial coefficients become well-determined. Note that the polynomials (A.4) and (A.5) reduce to (23) and (24) for the 2D case when $z = 0$ and $c_{xyz} = 0$. Matching Eqs. (A.4)–(A.6) at the boundaries with Eqs. (A.1)–(A.3) gives the following solutions for the coefficients

$$a_{xy} = \frac{a_y^{f_+} - a_y^{f_-}}{\Delta x}, \quad a_{xz} = \frac{a_z^{f_+} - a_z^{f_-}}{\Delta x}, \tag{A.8}$$

$$a_{yy} = \frac{a_{yy}^{f_+} + a_{yy}^{f_-}}{2}, \quad a_{xyy} = \frac{a_{yy}^{f_+} - a_{yy}^{f_-}}{\Delta x}, \tag{A.9}$$

$$a_{zz} = \frac{a_{zz}^{f_+} + a_{zz}^{f_-}}{2}, \quad a_{xzz} = \frac{a_{zz}^{f_+} - a_{zz}^{f_-}}{\Delta x}, \tag{A.10}$$

$$a_{yz} = \frac{a_{yz}^{f_+} + a_{yz}^{f_-}}{2}, \quad a_{xyz} = \frac{a_{yz}^{f_+} - a_{yz}^{f_-}}{\Delta x}, \tag{A.11}$$

$$b_{xy} = \frac{b_x^{f_+} - b_x^{f_-}}{\Delta y}, \quad b_{yz} = \frac{b_z^{f_+} - b_z^{f_-}}{\Delta y}, \tag{A.12}$$

$$b_{xx} = \frac{b_{xx}^{f_+} + b_{xx}^{f_-}}{2}, \quad b_{xxy} = \frac{b_{xx}^{f_+} - b_{xx}^{f_-}}{\Delta y}, \tag{A.13}$$

$$b_{zz} = \frac{b_{zz}^{f_+} + b_{zz}^{f_-}}{2}, \quad b_{yzz} = \frac{b_{zz}^{f_+} - b_{zz}^{f_-}}{\Delta y}, \tag{A.14}$$

$$b_{xz} = \frac{b_{xz}^{f_+} + b_{xz}^{f_-}}{2}, \quad b_{xyz} = \frac{b_{xz}^{f_+} - b_{xz}^{f_-}}{\Delta y}, \tag{A.15}$$

$$c_{xz} = \frac{c_x^{f_+} - c_x^{f_-}}{\Delta z}, \quad c_{yz} = \frac{c_y^{f_+} - c_y^{f_-}}{\Delta z}, \tag{A.16}$$

$$c_{xx} = \frac{c_{xx}^{f_+} + c_{xx}^{f_-}}{2}, \quad c_{xxz} = \frac{c_{xx}^{f_+} - c_{xx}^{f_-}}{\Delta z}, \tag{A.17}$$

$$c_{yy} = \frac{c_{yy}^{f_+} + c_{yy}^{f_-}}{2}, \quad c_{yyz} = \frac{c_{yy}^{f_+} - c_{yy}^{f_-}}{\Delta z}, \tag{A.18}$$

$$c_{xy} = \frac{c_{xy}^{f_+} + c_{xy}^{f_-}}{2}, \quad c_{xyz} = \frac{c_{xy}^{f_+} - c_{xy}^{f_-}}{\Delta z}, \tag{A.19}$$

$$a_{xx} = -(b_{xy} + c_{xz}), \quad a_{xxx} = -(b_{xxy} + c_{xxz}), \tag{A.20}$$

$$b_{yy} = -(a_{xy} + c_{yz}), \quad b_{yyy} = -(a_{xyy} + c_{yyz}), \tag{A.21}$$

$$c_{zz} = -(a_{xz} + b_{yz}), \quad c_{zzz} = -(a_{xzz} + b_{yzz}), \tag{A.22}$$

$$a_{xxy} = b_{xyy} = -\frac{c_{xyz}}{2}, \quad a_{xxz} = c_{xzz} = -\frac{b_{xyz}}{2}, \quad b_{yyz} = c_{yzz} = -\frac{a_{xyz}}{2}, \tag{A.23}$$

$$a_y = \frac{a_y^{f_+} + a_y^{f_-}}{2} - \frac{1}{8}a_{xxy}(\Delta x)^2, \quad a_z = \frac{a_z^{f_+} + a_z^{f_-}}{2} - \frac{1}{8}a_{xxz}(\Delta x)^2, \tag{A.24}$$

$$b_x = \frac{b_x^{f_+} + b_x^{f_-}}{2} - \frac{1}{8}b_{xyy}(\Delta y)^2, \quad b_z = \frac{b_z^{f_+} + b_z^{f_-}}{2} - \frac{1}{8}b_{yyz}(\Delta y)^2, \tag{A.25}$$

$$c_x = \frac{c_x^{f_+} + c_x^{f_-}}{2} - \frac{1}{8}c_{xzz}(\Delta z)^2, \quad c_y = \frac{c_y^{f_+} + c_y^{f_-}}{2} - \frac{1}{8}c_{yzz}(\Delta z)^2, \tag{A.26}$$

$$a_0 = \frac{a_0^{f_+} + a_0^{f_-}}{2} - \frac{1}{8}a_{xx}(\Delta x)^2, \quad a_x = \frac{a_0^{f_+} - a_0^{f_-}}{\Delta x} - \frac{1}{24}a_{xxx}(\Delta x)^2, \tag{A.27}$$

$$b_0 = \frac{b_0^{f_+} + b_0^{f_-}}{2} - \frac{1}{8}b_{yy}(\Delta y)^2, \quad b_y = \frac{b_0^{f_+} - b_0^{f_-}}{\Delta y} - \frac{1}{24}b_{yyy}(\Delta y)^2, \tag{A.28}$$

$$c_0 = \frac{c_0^{f_+} + c_0^{f_-}}{2} - \frac{1}{8}c_{zz}(\Delta z)^2, \quad c_z = \frac{c_0^{f_+} - c_0^{f_-}}{\Delta z} - \frac{1}{24}c_{zzz}(\Delta z)^2. \tag{A.29}$$

References

[1] J. Balbás, E. Tadmor, Non-oscillatory central schemes for one- and two-dimensional MHD equations, SIAM J. Sci. Comput. 28 (2) (2006) 533–560.

[2] J. Balbás, E. Tadmor, C.-C. Wu, Non-oscillatory central schemes for one- and two-dimensional MHD equations: I, J. Comput. Phys. 201 (2004) 261–285.
[3] D.S. Balsara, D.S. Spicer, A staggered mesh algorithm using high order Godunov fluxes to ensure solenoidal magnetic field in magnetohydrodynamics simulations, J. Comput. Phys. 149 (1999) 270–292.
[4] D.S. Balsara, Divergence-free adaptive mesh refinement for magneto-hydrodynamics, J. Comput. Phys. 174 (2001) 614–648.
[5] D.S. Balsara, Second order accurate schemes for magneto-hydrodynamics with divergence-free reconstruction, ApJ. Suppl. 151 (2004) 149–184.
[6] D.S. Balsara, J.S. Kim, A comparison between divergence-cleaning and staggered-mesh formulation for numerical MHD, ApJ 602 (2004) 1079.
[7] T.J. Barth, On the role of involutions in the discontinuous Galerkin discretization of Maxwell and magneto-hydrodynamics systems, in: D.N. Arnold, P.B. Bochev, R.B. Lehoucq, R.A. Nicolaides, M. Shashkov (Eds.), Compatible Spatial Discretizations, The IMA Volumes in Mathematics and its Applications, vol. 142, Springer-Verlag, New York, 2007, pp. 69–88.
[8] J.U. Brackbill, D.C. Barnes, The effect of nonzero $\nabla \cdot B$ on the numerical solution of the magnetohydrodynamic equations, J. Comput. Phys. 35 (1980) 426.
[9] M. Brio, C.C. Wu, An upwinding differencing schemes for the equations for ideal Magneto-hydrodynamics, J. Comput. Phys. 75 (1988) 400.
[10] W. Dai, P.R. Woodward, A simple finite difference scheme for multidimensional magnetohydrodynamics, J. Comput. Phys. 142 (1998) 331–369.
[11] A. Dedner, F. Kemm, D. Kroner, C.D. Munz, T. Schnitzer, M. Wesenberg, Hyperbolic divergence-cleaning for the MHD equations, J. Comput. Phys. 175 (2002) 645.
[12] T.A. Gardiner, J.M. Stone, An unsplit Godunov method for ideal MHD via constrained transport, J. Comput. Phys. 205 (2005) 509–539.
[13] G.S. Jiang, E. Tadmor, Non-oscillatory central schemes for multi-dimensional hyperbolic conservation laws, SIAM J. Sci. Comput. 19 (1998) 1892–1917.
[14] G.S. Jiang, C.-C. Wu, A high-order WENO finite difference scheme for the equations of ideal Magneto-hydrodynamics, J. Comput. Phys. 150 (1999) 561–594.
[15] D. Levy, G. Puppo, G. Russo, A third order central WENO scheme for 2D conservation laws, Appl. Numer. Math. 33 (2000) 407–414.
[16] S. Li, H. Li, A modern code for solving magnetohydrodynamics or hydrodynamic equations, Technical Report LA-UR-03-8925, Los Alamos National Laboratory, 2003.
[17] Y. Liu, Central schemes on overlapping cells, J. Comput. Phys. 209 (2005) 82–104.
[18] Y. Liu, C.-W. Shu, E. Tadmor, M. Zhang, Non-oscillatory hierarchical reconstruction for central and finite-volume schemes, Commun. Comput. Phys. 2 (2007) 933–963.
[19] X.D. Liu, E. Tadmor, Third order nonoscillatory central scheme for hyperbolic conservation laws, Numer. Math. 79 (1998) 397–425.
[20] X.D. Liu, S. Osher, Convex ENO high order multi-dimensional schemes without field by field decomposition or staggered grid, J. Comput. Phys. 141 (1998) 1–27.
[21] P. Londrillo, L. Del Zanna, High-order upwinding schemes for multidimensional magnetohydrodynamics, Astrophys. J. 530 (2000) 508.
[22] P. Londrillo, L. Del Zanna, On the divergence-free condition in Godunov-type schemes for ideal magneto-hydrodynamics: the upwinding constrained transport method, J. Comput. Phys. 195 (2004) 17–48.
[23] H. Nessyahu, E. Tadmor, Non-oscillatory central differencing for hyperbolic conservation laws, J. Comput. Phys. 87 (1990) 408–463.
[24] K.G. Powell, An approximate Riemann solver for MHD (that actually works in more than one dimension), Technical Report N0. 94-24, ICASE, Langley VA, 1994.
[25] J. Qiu, C.-W. Shu, On the construction, comparison, and local characteristic decomposition for high-order central WENO schemes, J. Comput. Phys. 183 (2002) 187–209.
[26] J. Rossmanith, An unstaggered high resolution constrained transport method for magneto-hydrodynamic flow, SIAM J. Sci. Comput. 28 (2006) 1766–1797.
[27] D. Ryu, F. Miniati, T.W. Jones, A. Frank, A divergence-free upwinding code for multi-dimensional MHD flows, Astrophys. J. 509 (1998) 244–255.
[28] C.W. Shu, S.J. Osher, Efficient implementation of essentially non-oscillatory shock capturing schemes II, J. Comput. Phys. 83 (1989) 32–78.
[29] Gabor Tóth, The $\nabla \cdot B = 0$ constraint in shock-capturing magnetohydrodynamics codes, J. Comput. Phys. 161 (2000) 605–652.
[30] G. Tóth, P.L. Roe, Divergence- and curl-preserving prolongation and restriction formulas, J. Comput. Phys. 180 (2002) 736–750.
[31] P.R. Woodward, P. Colella, The numerical simulation of two-dimensional fluid with strong shocks, J. Comput. Phys. 54 (1984) 115–173.
[32] U. Ziegler, A central-constrained transport scheme for ideal magneto-hydrodynamics, J. Comput. Phys. 196 (2004) 393–416.